Targeted Photodynamic Therapy using a Vectorized Photosensitizer coupled to Folic Acid Analog induces Ovarian Tumor Cell Death and inhibits IL-6-mediated Inflammation

Léa Boidin, Morgane Moinard, Albert Moussaron, Margaux Merlier, Olivier Moralès, Guillaume Paul Grolez, Martha Baydoun, Amirah Mohd-Gazzali, Mohammad Hafizie Dianel Mohd Tazizi, Hassan Hadi Abd Allah, et al.

Journal of Controlled Release 371 (2024) 351–370

Contents lists available at ScienceDirect

Journal of Controlled Release

journal homepage: www.elsevier.com/locate/jconrel

Targeted Photodynamic Therapy using a Vectorized Photosensitizer coupled to Folic Acid Analog induces Ovarian Tumor Cell Death and inhibits IL-6-mediated Inflammation

Léa Boidin [a,1], Morgane Moinard [b,1], Albert Moussaron [b,c,1], Margaux Merlier [a], Olivier Moralès [a,d], Guillaume Paul Grolez [a], Martha Baydoun [a], Amirah Mohd-Gazzali [e], Mohammad Hafizie Dianel Mohd Tazizi [e], Hassan Hadi Abd Allah [e], Yohan Kerbage [a], Philippe Arnoux [b], Samir Acherar [c,***,1], Céline Frochot [b,**,1], Nadira Delhem [a,*,1]

[a] Univ. Lille, Inserm, CHU Lille, U1189-ONCOTHAI-Assisted Laser Therapy and Immunotherapy for Oncology, Lille F-59000, France
[b] Univ. Lorraine, CNRS, UMR7274 – LRGP- Laboratoire des Réactions et Génie des Procédés, Nancy F-54000, France
[c] Univ. Lorraine, CNRS, UMR7375 – LCPM - Laboratoire de Chimie-Physique Macromoléculaire, Nancy F-54000, France
[d] Univ. Lille, CNRS, Inserm, CHU Lille, UMR9020-U1277 - CANTHER – Cancer Heterogeneity Plasticity and Resistance to Therapies, Lille F-59000, France
[e] School of Pharmaceutical Sciences, Universiti Sains Malaysia, Penang 11800, Malaysia

ARTICLE INFO

Keywords:
Photodynamic therapy
Epithelial Ovarian Cancer
Vectorized photosensitizer
Folic acid
IL-6

ABSTRACT

Ovarian cancer (OC) is one of the most lethal cancers among women. Frequent recurrence in the peritoneum due to the presence of microscopic tumor residues justifies the development of new therapies. Indeed, our main objective is to develop a targeted photodynamic therapy (PDT) treatment of peritoneal carcinomatosis from OC to improve the life expectancy of cancer patients. Herein, we propose a targeted-PDT using a vectorized photosensitizer (PS) coupled with a newly folic acid analog (FAA), named PS^{FAA}, in order to target folate receptor alpha (FRα) overexpressed on peritoneal metastasis.

This PS^{FAA} was the result of the coupling of pyropheophorbide-*a* (Pyro-*a*), as the PS, to a newly synthesized FAA *via* a polyethylene glycol (PEG) spacer. The selectivity and the PDT efficacy of PS^{FAA} was evaluated on two human OC cell lines overexpressing FRα compared to fibrosarcoma cells underexpressing FRα.

Final PS^{FAA}, including the synthesis of a newly FAA and its conjugation to Pyro-*a*, was obtained after 10 synthesis steps, with an overall yield of 19%. Photophysical properties of PS^{FAA} in EtOH were performed and showed similarity with those of free Pyro-*a*, such as the fluorescence and singlet oxygen quantum yields (Φ_f = 0.39 and Φ_Δ = 0.53 for free Pyro-*a*, and Φ_f = 0.26 and Φ_Δ = 0.41 for PS^{FAA}). Any toxicity of PS^{FAA} was noticed. After light illumination, a dose-dependent effect on PS concentration and light dose was shown. Furthermore, a PDT efficacy of PS^{FAA} on OC cell secretome was detected inducing a decrease of a pro-inflammatory cytokine secretion (IL-6).

This new PS^{FAA} has shown promising biological properties highlighting the selectivity of the therapy opening new perspectives in the treatment of a cancer in a therapeutic impasse.

1. Introduction

Among cancers occurring in women, ovarian cancer (OC) retains a fearsome reputation. It's still relatively rare, but its seriousness should not be underestimated, as it's the second most deadly cancer type of gynecological cancer [1]. This high mortality rate can be explained by

* Correspondence to: Nadira Delhem, INSERM-U1189-Unité OncoThAI., Institut de Recherche sur le Cancer ONCOLILLE, Bd du Professeur Jules Leclercq, Lille 59000, France.
** Correspondence to: Céline Frochot, LRGP UMR 7274 CNRS-UL, 1 rue Grandville, Nancy 54000, France.
*** Correspondence to: Samir Acherar, LCPM UMR 7375 CNRS-UL, 1 rue Grandville, Nancy 54000, France.
E-mail addresses: samir.acherar@univ-lorraine.fr (S. Acherar), celine.frochot@univ-lorraine.fr (C. Frochot), nadira.delhem@univ-lille.fr, nadira.delhem@inserm.fr (N. Delhem).
[1] contributed equally

https://doi.org/10.1016/j.jconrel.2024.05.033
Received 15 December 2023; Received in revised form 10 May 2024; Accepted 19 May 2024
Available online 5 June 2024

the asymptomatic and silent growth of the tumor and the lack of early screening and detection methods [2]. Epithelial Ovarian Cancer (EOC) accounts for >90% of ovarian tumors and remains a difficult cancer to treat [3].

Indeed, it is usually diagnosed at an advanced stage (FIGO stage III or IV) when extensive peritoneal metastases (PM) are present within the abdominal cavity [4]. Surgical removal of all PM, called complete macroscopic cytoreductive surgery (CRS) or debulking surgery, is usually performed in combination with platinum-based chemotherapy [5,6].

Despite these best upfront treatments, 70% of women with advanced disease develop peritoneal recurrence within 5 years [7]. This peritoneal recurrence may be due to the persistence of microscopic peritoneal metastases (mPM) that have not been removed by surgery or controlled by chemotherapy [8]. Furthermore, the EOC microenvironment is an inflammatory and immunosuppressive environment characterized by the presence of high levels of key immunoregulatory cytokines, chemokines and growth factors that promote ovarian tumorigenesis, cancer progression and resistance to chemotherapies [9]. Among these cytokines, higher levels of IL-10 and IL-6 were found in the serum and ascites of patients with EOC compared to patients with other malignancies [10,11]. The overexpression of these cytokines has been shown to correlate with a more aggressive tumor phenotype, the extent of disease and poor clinical outcome [12–14]. Similarly, IL-6 is capable of inducing multiple pathways leading to tumor proliferation, angiogenesis and chemoresistance [15]. Given the importance of IL-6 in the spread of EOC, a Phase II clinical trial has already evaluated the effect of the anti-IL-6 monoclonal antibody “siltuximab” [16]. Results showed that the antibody was well tolerated, but no complete response was found. Only targeting the IL-6 receptor seems insufficient to improve patient prognosis.

Therefore, a strategy capable of modulating the inflammatory microenvironment of EOC in concert with the eradication of residual metastases would be needed to improve patient prognosis and survival.

For such a purpose, the use of therapeutic targeting strategies, such as Photodynamic Therapy (PDT), would be relevant. Since 2005, our team developed some targeted photosensitizers (PSs) for PDT [17]. In fact, after the administration of a photosensitive molecule (PS) that accumulates in the targeting tissue, light illumination at an appropriate wavelength can induce fluorescence phenomenon, or photochemical reactions leading to the generation of reactive oxygen species (ROS), including singlet oxygen ($^1O_2$). This important oxidative stress induces a direct cytotoxic phenomenon on tumor cells and destruction of tumor vasculature [18]. In addition, releases of damage-associated molecular patterns (DAMPs) by damaged cells caused by PDT activate innate immunity thus promoting an antitumoral immune response [19]. Therefore, the fluorescence properties of the PS could improve the removal of peritoneal carcinosis by fluorescence-guided surgery, and the PDT effect would eradicate tumor metastasis and promote antitumor immune response.

In 2011, Van Dam and colleagues reported the use of fluorescein coupled to a folate that specifically targets the folate receptor alpha (FRα) to perform fluorescence guided surgery [20]. In late 2021, the Food and Drug Administration (FDA) approved pafolacianine (or OTL38) for the detection of malignant OC lesions which consists of a near-infrared (NIR) fluorescent dye coupled to folic acid (FA) [21].

Furthermore since a decade, PDT has been applied to cure many diseases [22] such as Age-Related Macular Degeneration (AMD), actinic keratosis, Barrett's esophagus, and various cancers (prostate, glioblastoma…). More interestingly, the use of PDT for EOC has also already been evaluated in Phase I and II clinical trials [23–25]. Unfortunately, authors reported severe morbidity such as digestive perforation, capillary leak syndrome, and pleural effusion added to no significant objective complete response or long-term tumor control.

Therefore, these clinical assays demonstrated the feasibility of intraperitoneal PDT after cytoreductive surgery, but the lack of tumor specificity for PS uptake may account for the low efficiency observed. Based on these studies, precise targeting of residual cancer cells by PS is required to enable intraperitoneal PDT for EOC. The FRα appears to be a promising target that would allow the targeting of a PS to EOC cells. Our recent study has shown that FRα was expressed in 75% of women suffering from EOC and presenting mPM after complete macroscopic cytoreductive surgery [26]. These results strengthened the idea of targeting the FRα using a targeted therapy such as PDT *via* a third-generation PS, which consisted of PS coupled to a ligand such as Folic Acid (FA).

Over the last few years, particular attention has been focused on the synthesis of new third-generation PSs using FA as ligand. In 2017, we published new FA-Spacer-PSs for anticancer targeted-PDT [27] and we noted that their photostability depends strongly on the nature of the PS conjugated to FA. Our most photostable FA-Spacer-PS (*i.e.*, FA conjugated to pyropheophorbide-*a* (Pyro-*a*) *via* a polyethylene glycol (PEG) type spacer, named FA-S-Pyro, has been patented (patent WO/2019/016397) for fluorescence detection and PDT treatment of PM [28,29]. Generally, the FA degradation studies described in the literature only consider one parameter (pH, temperature, light or O_2 …). In 2016, we wrote a review grouping all these crucial parameters and it clearly appears that two labile links are involved in the FA degradation [30]. Therefore, the integration of the FA degradation issue into the development of new FA-targeted compounds is crucial. In this study, we synthesize a totally new FA analog (FAA) as a stable FRα-targeting agent that should overcome the problem of FA degradation, thanks to molecular modeling and rational chemical modification. As far as we know, it is the first time that a new FAA is designed to address this issue and to be used for targeted PDT. This is an original strategy since the new FAA is conceived as FRα-targeting agent, which is not the case of the known FAA methotrexate used as FA antagonist (*i.e.*, antifolate) inhibiting FA metabolism.

This ambitious interdisciplinary study aims to design a new stable FAA coupled to a PS for the PDT treatment of mPM, which is shielded from degradation and can also provide an effective FRα-targeted PDT treatment while modulating the microenvironment of EOC. The proposed approach is an amalgamation of several different technologies, including molecular docking, chemical synthesis, stability and affinity studies, and *in vitro* biological testing.

2. Material and methods

2.1. Modeling

The human FRα crystal structure was obtained from the Protein Data Bank database (PDB ID: 4LRH). By using AutoDockTools (ADT), a graphical user interface available in the Autodock 4.2 software, FRα was loaded in PDB format, and all water molecules and heteroatoms were removed. Two ligands were evaluated in the molecular docking study, which are FA and a newly FAA. Both ligands were subjected to energy minimization using Molecular Mechanics 2 (MM2) force field by PerkinElmer Chem3D 17.1.

Polar hydrogens and Kollman charges were added to the receptor, while Gasteiger charges were assigned to the ligands. The size of the grid box was 60 × 60 × 60 (x, y, and z axis) with a spacing of 0.375 Å. The docking was then executed using Lamarckian Genetic Algorithm. After completion of the docking for each ligand, the resultant conformations were ranked according to their lowest binding energy and clustered together if their root-mean-square deviation (RSMD) values were within 0.5 Å from one another. The lowest binding energy and hydrogen bonds (H-bonds) for FA and the newly FAA were identified. The conformation with the lowest free energy of binding (FEB) was then chosen to be visualized using Biovia Discovery Studio Visualizer for identifying the ligand interactions with the amino acid residues of the receptor.

For PS^{FAA}, the same ligand preparation as FAA was done with a grid box of 60 × 40 × 40 (x, y, and z axis) with a spacing of 0.375 Å since the

molecule is larger than FA and FAA. The docking was also executed using same algorithm and the resultant conformations were ranked according to their lowest binding energy which later to be compare with the FEB of FA and FAA.

The inhibition constant, Ki also being calculated to predict the dissociation behaviour or the selectivity of compound PS^{FAA} towards FRα and RFC (as control). For final visualisation, we use Biovia Discovery Studio Visualizer for defining the 2-D binding interaction and PyMOL™ 2.5.8 Copyright© Schrodinger, LLC for defining the 3-D binding interaction of FA, FAA and PS^{FAA}.

2.2. Chemicals

All commercial chemicals were used without further purifications. Pyropheophorbide *a* (Pyro-*a*) was purchased from PorphyChem (Dijon, France). 2-Ethoxy-1-ethoxycarbonyl-1,2-dihydroquinoline (EEDQ), *N*, *N*-diisopropylethylamine (DIPEA), methylglyoxal, sodium sulfite (Na_2SO_3), acetic anhydride (Ac_2O), acetic acid (AcOH), dibenzoyl peroxide (DBP), copper sulfate ($CuSO_4$), sodium ascorbate, trifluoroacetic acid (TFA), sodium hydroxide (NaOH), 1-ethyl-3-(3-dimethylaminopropyl)carbodiimide (EDC), 4-dimethylaminopyridine (DMAP), *N*-Boc-2,2′-(ethylenedioxy)diethylamine, *N*-*N*′-dicyclohexylcarbodiimide (DCC) were purchased from Sigma-Aldrich (St Louis, MO, USA). Sodium pyrosulfite ($Na_2O_5S_2$) and sodium azide (NaN_3) were purchased from Fluka (Buchs, Suisse). *N*-bromosuccinimide (NBS) was purchased from Alfa Aesar (Haverhill, MA, USA).

2.3. Compounds characterization

1D (^1H, ^{13}C) NMR spectra were recorded on a Brucker Advance III 400 MHz spectrophotometer. The spectra were recorded in deuterated solvant at room temperature ($T = 298$ K) and residual peak of deuterated solvant was used as internal reference. The chemical shifts (δ) are given in parts per million (ppm).

High resolution mass spectrometry (HRMS) experiments were performed on a microTOF Bruker (electrospray ionization ESI+, 50–1000 in low and 50–2500 in width).

2.4. Photophysical Experiments

Absorption spectra were recorded on a UV-3600 UV–visible double beam spectrophotometer (Shimadzu, Marne la Vallée, France).

Fluorescence spectra were recorded on a Fluorolog FL3–222 spectrofluorimeter (HoribaJobin Yvon, Longjumeau, France) equipped with 450 W Xenon lamp, a thermo-stated cell compartment (25 °C), a UV–visible photomultiplier R928 (Hamamatsu, Hamamatsu City, Japan) and an InGaAs infrared detector (DSS-16A020L Electro-Optical System Inc., Phoenixville, PA, USA).

Excitation beam was diffracted by a double ruled grating SPEX monochromator (1200 grooves/mm blazed at 330 nm). Emission beam was diffracted by a double ruled grating SPEX monochromator (1200 grooves/mm blazed at 500 nm). Singlet oxygen ($^1O_2$) emission was detected through a double ruled grating SPEX monochromator (600 grooves/mm blazed at 1 μm) and a long-wave pass (780 nm). All spectra were measured in 4 faces quartz cuves. All the emission spectra (fluorescence and $^1O_2$ luminescence) were displayed with the same absorbance (<0.2) with the lamp and photomultiplier correction.

The fluorescence quantum yield (Φ_f) was determined by the Eq. (1):

$$\phi_f = \phi_{f_0} \times \frac{I_f}{I_{f_0}} \times \frac{DO_0}{DO} \times \left(\frac{n}{n_0}\right)^2 \quad (1)$$

where Φ_f and Φ_{fo}, I_f and I_{fo}, DO and DO_o, n and n_o are the fluorescence quantum yields, the fluorescence intensities, the optical densities and the refraction indexes, respectively, of the sample and of the standard.

The standard used for Φ_f was the Pyro-*a* in EtOH with a φ_{fo} of 0.39 [31].

The $^1O_2$ quantum yield (Φ_Δ) was determined by the Eq. (2):

$$\phi_\Delta = \phi_{\Delta_0} \times \frac{I}{I_0} \times \frac{DO_0}{DO} \quad (2)$$

where Φ_Δ and $\Phi_{\Delta o}$, I and I_o, DO and DO_o are the $^1O_2$ quantum yields, the $^1O_2$ luminescence intensities and the optical densities, respectively, of the sample and of the standard.

The standard used for Φ_Δ was the Pyro-*a* in EtOH with a $\Phi_{\Delta 0}$ of 0.53 [31].

Time-resolved experiments were performed using for excitation: a pulsed laser diode emitting at 407 nm (LDH-P-C-400 M, FWHM <70 ps, 1 MHz) coupled with a driver PDL 800-D (both PicoQuant GmbH, Berlin, Germany) and for detection: an avalanche photodiode SPCM-AQR-15 (EG & G, Vaudreuil, Canada) coupled with a 650 nm long-wave pass filter as detection system. The acquisition was performed by a PicoHarp 300 module with a 4 channels router PHR-800 (both PicoQuant GmbH, Berlin, Germany). The fluorescence decays were recorded using the single photon counting method. Data were collected up to 1000 counts accumulated in the maximum channel and analyzed using Time Correlated Single Photon Counting (TCSPC) software Fluofit (PicoQuant GmbH, Berlin, Germany) based on iterative reconvolution using a Levensberg-Marquandt algorithm, enabling the obtention of multi-exponential profiles (mainly one or two exponentials in our cases).

$^1O_2$ lifetime measurements have been performed on a TEMPRO-01 spectrophotometer (Horiba Jobin Yvon, Longjumeau, France) composed with a pulsed diode excitation source SpectraLED-415 emitting at 415 nm, a cell compartment, a Seya-Namioka type emission monochromator (600–2000 nm) and a H10330–45 near-infrared photomultiplier tube with thermoelectric cooler (Hamamatsu, Hamamatsu City, Japan) as detection system. The system was monitored by a single photon-counting controller FluoroHub-B and the software DataStation and DAS6 (Horiba Jobin Yvon, Longjumeau, France).

2.5. Biological Experiments

2.5.1. Cell Lines

The selectivity of PS^{FAA} was evaluated on three cell lines: 2 OC cell lines (OVCAR3 and SKOV3) and one fibrosarcoma cell line (HT080). These three cell lines were ordered from the American Type Culture Collection (ATCC, Manassas, Virginia, USA). SKOV3 cells were cultured in 50% DMEM medium (4.5 g/L D-glucose, L-glutamine, Gibco, Thermo Fisher Scientific, Waltham, MA, USA) and 50% F-12 (Ham's F-12 Nutrient Mix, Gibco, Thermo Fisher Scientific, Waltham, MA, USA), OVCAR3 cells were cultured in RPMI-1640 medium (Gibco, Thermo Fisher Scientific, Waltham, MA, USA) and HT1080 cells were cultured in MEM medium (Gibco, Thermo Fisher Scientific, Waltham, MA, USA). The mediums were supplemented with 10% heat inactivated fetal calf serum (Gibco, Thermo Fisher Scientific, Waltham, MA, USA) and with 1% penicillin (Gibco, Thermo Fisher Scientific, Waltham, MA, USA). Cells were maintained in an incubator at 37 °C, 5% CO_2, and 95% humidity.

2.5.2. RNA extraction, Retro Transcription and Real-Time Quantitative PCR (RTqPCR)

2.5.2.1. RNA extraction. Total RNA from cultured cells (1.10^6 cells) was extracted using the Trizol® reagent (Life Technologies, Carlsbad, CA, USA) method according to the manufacturer's instructions. Briefly, cells were suspended in 1 mL of Trizol® and stored at −80 °C until further use. For RNA isolation, 200 μL of $CHCl_3$ were added to samples, then cells were centrifuged at 12000 *g* for 15 min at 4 °C. The upper transparent phase was taken up and total RNA was precipitated with 500 μL of *i*PrOH and stored at −80 °C for 10 min. Then, RNA was centrifuged at

12000 *g* for 15 min at 4 °C and the pellet of total RNA was washed with EtOH 70% which was then discarded and samples were left to dry at room temperature. Then samples were centrifuged at 7500 *g* for 15 min at 4 °C, and the pellet was suspended in 30 μL of RNAse and DNAse free water (Life Technologies, Carlsbad, CA, USA). RNA concentration and purity were measured by spectrophotometric methods using the NanoDrop 2000/2000c v.1.6.198 software (Thermo Scientific, Waltham, MA, USA). In order to be considered sufficiently pure, the minimum acceptable values of the specific absorbance ratios were: 260/280 $\geq$ 1.8; 260/230 $\geq$ 1.6. Pure concentrated RNA was stored at −80 °C until further use.

2.5.2.2. The qPCR program. 2 μg of total RNA were supplemented with 5 μL of a master mix: 1 μL oligo dT (8 nmol) (Roche Diagnostic, Meylan, France), 4 μL of RNAse/DNAse free water and 0,1 μL RNAsin (40 U/μL, Promega, Charbonnières, France). Then, samples were incubated at 70 °C for 10 min, followed by 5 min at room temperature. After this 10 μL of the reaction mix were added to samples: 6 μL buffer 5× (Tris-HCl, KCl, $MgCl_2$) (Invitrogen, UK) + 1 μL DiThioThreitol (DTT, 0.1 M) (Invitrogen, Waltham, USA) + 2 μL deoxyribose Nucleotide Tri-Phosphates (dNTPs, 10 mM) (Amersham Biosciences, Amersham, UK) + 0.1 μL RNAsin (40 U/μL, Promega, Charbonnières, France) + 1 μL Transcriptase Reverse Superscript™ (200 U/μL, Life Technologies, Carlsbad, CA, USA). Samples were first incubating at 45 °C for 60 min, followed by a second incubation at 95 °C for 5 min. Finally, ultrapure distilled water (GIBCO-Life Technologies, Carlsbad, CA, USA) was added to obtain a final concentration of 10 ng total complementary DNA (cDNA)/μL and stored at −80 °C until further use.

Transcripts were quantified using real-time quantitative RT-PCR with the Aria Mx system (Agilent Technologies, Santa Clara, California, USA), in PCR-96-LP-FLT plates (Corning Axygen®, Corning, USA). In each well, 10 μL of a specific couple of primers (Eurogentec, Seraing, Belgium) and 1 μL of cDNA sample (equivalent to 10 ng of RNA/μL) were added. PCR reactions were performed according to the manufacturer's instructions, in a final volume of 20 μL, using 2× MESA GREEN qPCR MasterMix Plus for SYBR® 258 Assay (Eurogentec, Seraing, Belgium). The pCR program included initial denaturation for 5 min at 95 °C, followed by 40 standard amplification cycles as followed: 15 s at 95 °C (denaturation) then 1 min at 60 °C (annealing and elongation). Fluorescent products were detected at the last step of each cycle.

Quantitative PCR reactions were used to quantify gene expression of FR*α*. The housekeeping genes: Glyceraldehyde-3-Phosphate DeHydrogenase (GAPDH), HyPoxanthine Guanine PhosphoRibosyl Transferase (HPRT) and β-actin were used as controls. All primers were designed for real-time PCR (Table 1) and purchased from (Eurogentec, Seraing, Belgium) or (Sigma-Aldrich, St Louis, MO, USA). Quantitative analysis was achieved based on the cycle threshold (Ct) and Ct value of each well was calculated using Agilent Aria Mx software V.1.71. The results were normalized by the mean of three housekeeping (HKG) genes Ct and data were represented as $1/\Delta Ct = 1$ / (Ct target gene – Ct HKG).

2.5.3. Western Blot

Cell lines were lysed in RIPA buffer consisting of 20 mM Tris-HCM, 50 mM NaCl, 5 mM EDTA, 1% Triton X-100, 0,02% sodium azide supplemented by a cocktail of protease inhibitors (Sigma-Aldrich, St Louis, MO, USA). After centrifugation (14,000 rpm, 30 min), cell debris were removed, and supernatants were collected. Protein concentrations were measured using Bio-Rad Protein Assay according to manufacturer's instructions (Biorad, Hercules, CA, USA).

20 μg of proteins were separated by SDS-PAGE electrophoresis using gradient pre-casts gels (NuPAGE®NOVEX 4–12% gradient, Bis-Tris, Life Technologies, Carlsbad, CA, USA). Then proteins were transferred on PVDF membrane (Immobilon-P™, Sigma-Aldrich, St Louis, MO, USA). The membrane was blocked for 2 h at room temperature in casein (2 g/L) blocking buffer, and then incubated overnight at 4 °C with primary antibodies [rabbit anti-human FR*α* mAb 1:1000 (Invitrogen, Thermo Fisher Scientific, Waltham, MA, USA); mouse anti-cyclophilin B mAb 1:1000 (Cell signaling Technology, Danvers, Massachussets, USA).

Membranes were washed with PBS-Tween 0.05%, and then incubated for 1 h at room temperature with peroxidase-conjugated secondary antibodies anti-mouse or anti-rabbit, 1:10000 (GE Healthcare, Wauwatosa, WI, USA). Specific protein signals were visualized using Western Lightning® Plus-ECL, Enhanced Chemiluminescence Substrate kit (Thermo Fisher Scientific, Waltham, MA, USA) and read by chemiluminescent with LAS-3000 (Fujifilm Global, USA) using the Image Lab software.

2.5.4. Flow cytometry

FRα expression was analyzed by cytometry on OVCAR3, SKOV3 and HT1080 cell lines. We used an anti-FR*α*-PE (BioLegend, San Diego, CA, USA) and its IgG2a-PE isotype control (Miltenyi Biotec, Bergisch Gladbach, Germany) to determine the FRα expression. A total of 10^5 cells were taken up in a volume of 200 μL of PBS −/− and the fragment crystallizable receptors (FCR) were blocked with FCR blocking reagent (Miltenyi Biotec, Bergisch Gladbach, Germany) for 15 min at 4 °C. They were then incubated for 15 min at 4 °C in the dark with 2 μL of each antibody. The labeled cells were filled up with 300 μL of PBS −/−. Samples were acquired using a Attune NxT (Thermo Fischer Scientific, Waltham, MA, USA) and Median fluorescence intensity (MFI) were analyzed using the Flow Jo software 10.0.7 (Tree Star Inc., Ashland, OR, USA).

2.5.5. Competition experiment

Adherent cells were cultured on glass coverslips in 12-well plates (Corning, Somerville, MA, USA). 24 h after plating, 4 mM of a FA (Folic Acid, Sigma – Aldrich, Saint-Louis, Missouri, USA) solution was added for different times (2 h, 6 h, 10 h and 24 h). After the corresponding incubation time of FA, cell monolayers were washed with PBS (Gibco, Thermo Fisher Scientific, Waltham, MA, USA) and incubated with PS^{FAA} for 24 h at 9 μM. Cells were then fixed with paraformaldehyde 4% (Santa Cruz Biotechnology, Dallas, TX, USA). After washing, the nuclei were counterstained with DAPI (Thermo Scientific, Waltham, MA, USA). Coverslips were mounted in Glycergel (Agilent Dako, C056330–2, Santa Clara, California, USA) and observed using a Leica TCS SP8 MP Multiphoton microscope (Leica, Wetzlar, Germany). Semi-quantification of the signal was performed using Fiji-ImageJ software V2.3.0/1.53q.

2.5.6. Microscale thermophoresis (MST)

2.5.6.1. FRα/RFC vs. FA/FAA. MST was conducted using a NT.115 Pico MST instrument (Nano Temper Technologies GmbH, Munich, Germany equipped with red and blue filter sets. FR*α* and RFC were diluted to 200 nM in PBS (Gibco, Thermo Fisher Scientific, Waltham, MA, USA) and labeled with Monolith His-Tag Labeling Kit RED-tris-NTA (Nano Temper

Table 1
List of the primers with their sequences in 5′ to 3′ direction.

	Forward Primer	Reverse Primer
FR*α*	AGGTGCCATCTCTCCACAGT	GAGGACAAGTTGCATGAGCA
B-actine	CACGGCATCGTCACCAACT	AGCCACACGCAGCTCATTG
GAPDH	GCCAAGGTCATCCATGACAACTTTGG	GCCTGCTTCACCACCTTCTTGATGTC
HPRT	CCTGGCGTCGTGATTAG	ATGGCCTCCCATCTCCTT

Technologies GmbH, Munich, Germany). The RED-tris-NTA dye was diluted in PBS-T to 100 nM. The mix was incubated at room temperature in the dark for 30 min. FA and FAA were diluted with a serial 1:1 ratio of 16 gradients. Then, the labeled protein and molecules were mixed separately with 1:1 ratio and incubated at room temperature. Capillaries were then filled individually and loaded into the instrument. Data were acquired using medium MST power and 20% LED. Data were analyzed using MO Control Software (Nano temper Technologies GmbH, Munich, Germany). MST figures were rendered using MO Affinity Analysis (Nano Temper Technologies GmbH, Munich, Germany).

2.5.6.2. FRα/RFC vs. PS^{FAA}. MST was conducted using a NT.115 Pico MST instrument (Nano Temper Technologies GmbH, Munich, Germany) equipped with red and blue filter sets. FRα and RFC were diluted with a serial 1:1 ratio of 16 gradients. Since molecules were naturally fluorescent, no labeling was required. Molecules were mixed separately with 1:1 ratio and incubated at room temperature. Capillaries were then filled individually and loaded into the instrument. Data were acquired using medium MST power and 20% LED. Data were analyzed using MO Control Software (Nano Temper Technologies GmbH, Munich, Germany). MST Figures were rendered using MO Affinity Analysis (Nano Temper Technologies GmbH, Munich, Germany).

2.5.7. Confocal microscopy

For immunofluorescence, adherent cells were cultured on glass coverslips in 12-well plates (Corning, Somerville, MA, USA). 24 h after plating, 9 μM of PS^{FAA} were added to the wells during 24 h. Then, the cell monolayers were washed with PBS (Gibco, Thermo Fisher Scientific, Waltham, MA, USA) and cells were fixed with paraformaldehyde 4% (Santa Cruz Biotechnology, Dallas, TX, USA). The cells were washed three times with PBS (Gibco, Thermo Fisher Scientific, Waltham, MA, USA) and then incubated for 1 h at room temperature in PBS containing gelatin (1.2%), glycine (0.2 M) and tween-20 (0.05%) (Sigma-Aldrich, St Louis, MO, USA) for blocking. After washing, the cells were incubated for 1 h with the primary FRα polyclonal antibody (Rabbit/IgG) (Invitrogen, Thermo Fisher Scientific, Waltham, MA, USA), diluted (1:400) in PBS (Gibco, Thermo Fisher Scientific, Waltham, MA, USA) one night at 4 °C. Cells were washed three times with PBS (Gibco, Thermo Fisher Scientific, Waltham, MA, USA) and then incubated with the secondary antibody Alexa Fluor 555 (Invitrogen, Thermo Fisher Scientific, Waltham, MA, USA) (1:300) diluted in PBS (Gibco, Thermo Fisher Scientific, Waltham, MA, USA) for 1 h at room temperature. After washing, the nuclei were counterstained with DAPI (Thermo Fisher Scientific, Waltham, MA, USA). Coverslips were mounted in Glycergel (Agilent Dako, C056330–2, Santa Clara, California, USA, USA) and observed using a LSM 710 inverted confocal microscope (Leica, Wetzlar, Germany). Photographic images were resized, organized, and labeled using Fiji-ImageJ software V2.3.0/1.53q. Semi-quantification was also performed to allow for comparison, all images were taken with the same microscope settings. Images were converted into 8-bit. Thresholding of images was performed to detect only PS^{FAA}. Note that the value of the threshold was conserved and used for each analyzed cell. Finally, the "analyze particles" plug-in was used to count the total intensity of the PS^{FAA} and FRα.

2.5.8. Fluorimetry Assay

4000 cells per 150 μL of media for each cell line were seeded in a white wall 96-well plate (Corning, Somerville, MA, USA) in triplicate. 24 h after seeding, PS^{FAA} was added to the wells with various concentrations from 0 to 9 μM (0, 0.45, 0.9, 1.8, 4.5 and 9 μM) for varying incubation time points (0, 1, 3, 6, 12 and 24 h). Throughout the experiment, the cells remained in total darkness. At the end of incubation period, the media was removed, cells were washed with PBS (Gibco, Thermo Fisher Scientific, Waltham, MA, USA) two times and fresh media was then added to the cells to measure the intracellular levels of PS^{FAA}. Non-treated controls, containing no PS^{FAA}, were carried out. PS^{FAA} fluorescence was measured with an excitation wavelength of 412 ± 10 nm and an emission wavelength of 668 nm ± 10 nm, by using ClarioStar Plus (BMG Labtech, Champigny sur Marne, France) driven by MARS™ Software v2.06. The results were expressed in Relative Fluorescence Unit (RFU).

2.5.9. LDH based Cytotoxicity Assay

Briefly, 4000 cells per 150 μL of media for each cell line were seeded in a 96-well culture plate (Corning, Somerville, MA, USA) in triplicate. After 24 h, the medium was replaced by 100 μL of fresh one containing PS^{FAA} at different concentrations from 0 to 9 μM (0, 0.14, 0.28, 0.56, 1.12, 2.25, 4.5 and 9 μM). Cells treated with 2% Triton X-100 (Sigma-Aldrich, St Louis, MO, USA) for 2 h was used as a positive control of cytotoxicity (Positive Control Well Condition) and a solution of DMSO at 10 μL/1 mL of media was used as media control (Media control condition). 24 h after plating, plates were centrifuged (300 *g*, 10 min) and a multichannel was used to transfer 100 μL of supernatants in a new plate. 100 μL of the mixed cytotoxic detection kit reagent was added to each well on the top of the supernatant (Roche, Sigma Aldrich, St Louis, MO, USA) after having prepared it according to the manufacturer's protocol. The assay plates were then incubated at room temperature in the dark for 20 min. After which they were read using a ClarioStar Plus (BMG Labtech, Champigny sur Marne, France) reader once at 492 nm (background values) and another time at 595 nm (assay values). Media without cells were used to serve as blank and values were subtracted to each well. Values 492 nm were subtracted to values of 595 nm to get the Assay Well Condition. The cytotoxicity was calculated as Relative Cytotoxicity (%) = ((Assay Well Condition - Media Control Condition) / (Positive control Well Condition - Media Control condition)) x 100, results were expressed in percent.

2.5.10. Photodynamic therapy protocol

4000 cells per 150 μL of media for each cell line were seeded in a white wall 96-well plate (Corning, Somerville, MA, USA) in triplicate. After 24 h, the medium was replaced by a fresh one containing PS^{FAA} at different concentrations from 0 to 9 μM (0, 0.14, 0.28, 0.56, 1.12, 2.25 and 4.5 μM). 24 h later, the medium containing PS^{FAA} was changed and replaced by the normal medium of the cell type after two washing steps with PBS (Gibco, Thermo Fisher Scientific, Waltham, MA, USA). A homogeneous illumination (1 mW/cm^2) was then performed at different light doses (1.8, 0.9 and 0.3 J/cm^2) with a specific 672 nm laser-based device developed by our OncoThAI research unit [32]. All the experiments were performed in dark conditions.

2.5.11. Viability Assay

Cancer cell lines viability after PDT was assessed by a viability assay based on mitochondrial metabolism. 24 h post-PDT, 100 μL/well of the Celltiter-Glo mix (CellTiterGlo®, Promega, Madison, WI, USA) was added at room temperature for 10 min and protected from light according to the manufacturer's instructions. The bioluminescence was then read using a luminometer ClarioStar Plus (BMG Labtech, Champigny sur Marne, France) driven by MARS™ Software v2.06. Half Maximal Effective Concentration (EC_{50}) according to the light dose and the different cell lines was calculated from the viability curves using nonlinear regression with GraphPad Prism Software (Version 8.2.1). Results were normalized over the non-treated condition (NT) and expressed in percent.

2.5.12. Proliferation Assay

Human blood samples were collected from healthy adult donors after obtaining informed consent, in accordance with the approval of the Institutional Review Board at the Biology Institute of Lille (DC-2013-1919). Peripheral Blood Mononuclear cells (PBMCs) were isolated from peripheral blood samples by density gradient centrifugation using lymphocyte separation medium (Eurobio, Les Ullis, France) and

leucosep 50 mL tubes (Eurobio, Les Ullis, France). 100,000 PBMCs per well were cultured in a ML10 medium made with RPMI 1640 medium supplemented with sodium pyruvate (1 mM), non-essential amino acids MEM 1×, HEPES (25 mM), 2-mercaptoethanol (50 μM), gentamicin (10 μg/mL) (Thermo Fisher Scientific, Waltham, MA, USA), and 10% SVF (Gibco, Thermo Fisher Scientific, Waltham, MA, USA). Cells were activated or not with plated anti-CD3 (1 μg/mL; Miltenyi, Bergisch Gladbach, Germany) and anti-CD28 (100 ng/mL; Clinisciences, Montrouge, France). 50 μL of cancer cell line supernatant treated according to different conditions (NT: non treated, PS^{FAA}: PS^{FAA} only at 9 μM, illu: illumination only at 3.6 J/cm^2, PDT: illumination in the presence of 9 μM PS^{FAA} and illuminated at 3.6 J/cm^2 and ML10: raw culture media of PBMCs), also called conditioned media, was added to PBMCs in 96 round-bottomed plates when stated.

Proliferation assays were set up in a round-bottom 96-well plate (Corning, Somerville, MA, USA) in triplicate and measured by adding radioactive [3H] thymidine (1 μCi/well) (PerkinElmer, Courtaboeuf, France) to each well 18 h before harvesting. At the end of the culture, the cells were harvested on a glass fiber filter (PerkinElmer, Courtaboeuf, France) using a Tomtec harvester (Wallac, Turku, Finland), then sealed in a sample bag (PerkinElmer, Courtaboeuf, France) with scintillation liquid (Beckman Coulter, Brea, CA, USA). Radioactive thymidine was measured by scintillation counting using a β-counter (1450 Trilux, Wallac, Finland). Proliferation was estimated in count per minute (CPM) and pressed in CPM or normalized CPM. Normalized CPM = CPM of the sample/Average CPM of Non-Treated control.

2.5.13. ELISA

To analyze the impact of PDT on cancer cells secretoma, cells were treated with PDT according to 4 conditions: Untreated cells (NT), cells treated with 9 μM of PS^{FAA} without illumination (PS), cells treated with illumination at 3.6 J/cm^2 without PS^{FAA} (Illu) and cells treated with PS^{FAA} and subjected to illumination at 3.6 J/cm^2 (PDT). Conditioning media were recovered 6, 24, 48 and 72 h after PDT to determine cytokines secretion by the Sandwich ELISA (Enzyme-Linked ImmunoSorbent Assay) method. Interleukine(IL)-2, 6, 10, TNFα, TGFβ, IFNγ concentrations were investigated. Only cytokines detectable above the threshold were represented (IL-6 and TGFβ).

Briefly, primary purified antibodies (BD Pharmingen™, San Jose, CA, USA) were coated overnight at 4 °C in flat-bottomed 96-well maxisorp plates (NUNC, Thermo Fisher Scientific, Waltham, MA, USA). After washes with PBS-Tween 0.05% and a non-specific site blocking with PBS-BSA 3% (Bovine Serum Albumin, Sigma-Aldrich, St Louis, MO, USA) for 2 h at room temperature, culture supernatant was incubated in the plate overnight at 4 °C. After washes (PBS-Tween 0.05%), the corresponding biotinylated antibodies were added for protein detection (1 μg/mL) (BD Pharmingen™, San Jose, CA, USA) for 90 min at room temperature. After washes (PBS-Tween 0.05%), the reaction was amplified with Streptavidine-peroxydase to 1/10000 th (Interchim, Montluçon France) for 30 min at room temperature. Cytokines concentrations were finally highlighted with the addition of Ortho-Phenylenediamine Dihydrochloride (OPD) at 10 mg/mL (Sigma-Aldrich, St Louis, MO, USA). After colour development, the reaction was stopped by addition of HCl 2 N (VWR, Radnor, Pensylvania, USA, USA). The plates were then read using a ClarioStar Plus (BMG Labtech, Champigny sur Marne, France) at 492 nm powered by MARS™ Software v2.06.

2.6. Statistical analysis

All results were expressed as the means and standard deviations or standard error of the mean of triplicates of at least three independent experiments. All data were analyzed using the statistical package GraphPad Prism for Windows 3.0.1 (GraphPad, San Diego, CA, USA). The normality of the distributions was assessed using the Shapiro–Wilk test. All quoted p-values are two-sided, with $p \leq 0.05$ (*), $p \leq 0.01$ (**), $p \leq 0.001$ (***), and $p \leq 0.0001$ (****) being considered statistically significant for the first and highly significant for the other.

2.7. Chemical synthesis

Synthesis of di-*tert*-butyl propioloyl-*L*-glutamate **1**

H-Glu(O*t*-Bu)-O*t*Bu.HCl (450 mg, 1.52 mmol) was dissolved in freshly distilled DMF (9 mL). DIPEA (259 μL, 1.52 mmol), propiolic acid (106.6 mg, 1.52 mmol) and EEDQ (376.2 mg, 1.51 mmol) were added and the mixture was stirred overnight at r.t. The solution was concentrated and the residue was purified by preparative HPLC using acetonitrile/water (0.1% TFA; 10:90) to 100% acetonitrile gradient in 15 min, followed by isocratic acetonitrile for 10 min. Rt = 24.1 min. Pure product **1** was isolated as an orange oil that solidified upon standing (369 mg, 78%).

^{1}H NMR (400 MHz, DMSO-d_6): δ (ppm) = 1.39 (s, 6 x CH_3, 2 x t-Bu), 1.71–1.81 (m, CH, CH_2^{β}), 1.87–1.95 (m, CH, CH_2^{β}), 2.19–2.32 (m, CH_2, CH_2^{γ}), 4.07–4.17 (m, CH, CH^{α}), 4.17 (s, CH, C*H*alkyne), 9.01 (d, N*H*, J = 7.51 Hz).

^{13}C NMR (400 MHz, DMSO-d_6): δ (ppm) = 26.18 (*C*H_2^{β}), 28.03 (3 x *C*H_3), 28.17 (3 x *C*H_3), 31.48 (*C*H_2^{γ}), 52.53 (*C*H$^{\alpha}$), 76.91 (*C*alkyne), 78.27 (*C*alkyne), 80.29 (*t*-Bu-*C*quat), 81.40 (*t*-Bu-*C*quat), 152.23 (*C*=O), 170.58 (*C*=O), 171.69 (*C*=O).

Synthesis of 2-amino-6-methylpteridin-4(1*H*)-one **2**

To a suspension of 2,5,6-triamino-5,6-dihydropyrimidin-4(1H)-one sulfate (1:1) (2.41 g, 10 mmol) in water (200 mL), Na_2SO_3 (25.2 g, 200 mmol) was added with stirring at r.t. The resulting clear solution was cooled at 0 °C and a solution of methylglyoxal (1.80 g; 40% in water, 10 mmol) and $Na_2S_2O_5$ (1.14 g, 6 mmol) in water (5 mL) was added at 0 °C over a 30 min period. The resulting yellow mixture was allowed to reach room temperature, and the stirring was continued for further 16 h. The solid formed was filtered, washed with both water and ethanol and dried (100 °C, 4 h). The title compound **2** (1.73 g, 99%) was obtained as a yellow solid.

^{1}H NMR (400 MHz, D_2O): δ (ppm) = 2.11 (s, CH_3, pterin-C*H*$_3$), 8.19 (s, CH, pterin-*H7*).

The characterization of product **2** is consistent with that reported in the literature (Waring P., Armarego W. L. F. Aust. J. Chem., 1985, 38, 629–631).

Synthesis of *N*-(6-methyl-4-oxo-3,4-dihydropteridin-2-yl)acetamide **3**

2-Amino-6-methylpteridin-4(1H)-one **2** (0.5 g, 2.8 mmol) was refluxed in a 1:1 mixture of acetic acid and acetic anhydride (20 mL) for 2 h. After this time, the solid in suspension progressively disappeared leaving a colorless transparent solution. The resulting homogeneous solution was cooled and allowed to stand at room temperature overnight. The formed precipitate was filtered, washed with ether and the title compound **3** (555 mg, 91%) was obtained as a red solid.

^{1}H NMR (400 MHz, DMSO- *d6*): δ (ppm) = 2.20 (s, CH_3, C*H*$_3$CONH), 2.60 (s, CH_3, pterin-C*H*$_3$), 8.80 (s, CH, pterin-*H7*).

The characterization of product **3** is consistent with that reported in the literature. (Waring P., Armarego W. L. F. Aust. J. Chem., 1985, 38, 629–631).

^{13}C NMR (400 MHz, DMSO-d_6): δ (ppm) = 21.02 (pterin-*C*H_3), 23.90 (*C*H_3CONH), 130.25 (pterin-*C*), 148.79 (pterin-*C*), 150.59 (pterin-*C7*), 151.43 (pterin-*C*), 153.62 (pterin-*C*), 159.40 (pterin-*C*=O), 174.06 (CH_3*C*ONH).

Synthesis of *N*-(6-(bromomethyl)-4-oxo-3,4-dihydropteridin-2-yl) acetamide **4**

N-Acetyl pteridine derivative **3** (500 mg, 2.3 mmol) was dispersed in acetic acid (20 mL). NBS (609 mg, 3.4 mmol,) and dibenzoylperoxide (55 mg, 0.23 mmol) were added and this mixture was stirred and heated at 120 °C for 3 h. The progress of the reaction was monitored by analytical HPLC with a Pursuit 5-C18 column (2.5 μm, 4.6 × 250 mm; Varian) using acetonitrile/water (0.1% TFA; 10:90) to 100% acetonitrile gradient in 15 min, followed by isocratic acetonitrile for 10 min. After

cooled at r.t., the crude was diluted with CH_2Cl_2 and filtered through a celite pad. After evaporation of the solvent under vacuum, the residue was purified by preparative HPLC using acetonitrile/water (0.1% TFA; 10:90) to 100% acetonitrile gradient in 15 min, followed by isocratic acetonitrile for 10 min. *R*t = 12.3 min. Pure product was isolated as a greenish white powder (294 mg, 43%).

^{1}H NMR (400 MHz, DMSO-d_6): δ (ppm) = 2.23 (s, CH_3, C*H*$_3$CONH), 4.89 (s, CH_2, pterin-C*H*$_2$Br), 9.04 (s, CH, pterin-*H7*).

^{13}C NMR (400 MHz, DMSO-d_6): δ (ppm) = 23.95 (*C*H$_3$CONH), 31.24 (pterin-*C*H$_2$Br), 62.58 (pterin-*C*), 130.00 (pterin-*C*), 148.78 (pterin-*C7*), 149.18 (pterin-*C*), 154.25 (pterin-*C*), 159.43 (pterin-*C*=O), 174.15 (CH$_3$*C*ONH).

HRMS (ESI+): *m/z* calcd. For $C_9H_9BrN_5O_2$ $[M + H]^+$ 297.9940; found 297.9934.

Synthesis of *N*-(6-(azidomethyl)-4-oxo-3,4-dihydropteridin-2-yl) acetamide **5**

A mixture of **4** (35 mg, 0.11 mmol) and sodium azide (22 mg, 0.33 mmol) was dissolved in acetonitrile (10 mL). The reaction mixture was stirred at 70 °C for 4.5 h. The progress of the reaction was monitored by analytical HPLC with a Pursuit 5-C18 column (2.5 μm, 4.6 × 250 mm; Varian) using acetonitrile/water (0.1% TFA; 10:90) to 100% acetonitrile gradient in 15 min, followed by isocratic acetonitrile for 10 min. After evaporation of the solvent under vacuum, crude compound was obtained quantitatively and was directly reengaged in the next step.

^{1}H NMR (400 MHz, DMSO-d_6): δ (ppm) = 2.25 (s, CH_3, C*H*$_3$CONH), 4.70 (s, CH_2, pterin-C*H*$_2$N$_3$), 8.74 (s, CH, pterin-*H7*).

^{13}C NMR (400 MHz, DMSO-d_6): δ (ppm) = 25.36 (*C*H$_3$CONH), 52.94 (pterin-*C*H$_2$N$_3$), 130.48 (pterin-*C*), 145.72 (pterin-*C*), 148.37 (pterin-*C7*), 157.10 (pterin-*C*), 159.74 (pterin-*C*), 171.12 (pterin-*C*=O), 172.10 (CH$_3$*C*ONH).

HRMS (ESI+): *m/z* calcd. For $C_9H_9N_8O_2$ $[M + H]^+$ 261.0848; found 261,0779.

Synthesis of di-*tert*-butyl (1-(2-acetamido-4-oxo-3,4-dihydropteridin-6-yl)-1*H*-1,2,3-triazole-4-carbonyl)-*L*-glutamate **6**

The azide compound **5** (50 mg, 0.19 mmol) and the alkyne **1** (59 mg, 0.19 mmol) were suspended in a 2:2:1 mixture of water (2 mL), *tert*-BuOH (2 mL) and THF (1 mL) in a 10 mL glass vial equipped with a small magnetic stirring bar. To this was added copper sulphate solution (1 N, 19 μL) and sodium ascorbate (16 mg, 0.076 mmol). The mixture was then stirred at r.t. for 30 min. The progress of the reaction was monitored by analytical HPLC with a Pursuit 5-C18 column (2.5 μm, 4.6 × 250 mm; Varian) using acetonitrile/water (0.1% TFA; 10:90) to 100% acetonitrile gradient in 15 min, followed by isocratic acetonitrile for 10 min. After evaporation of the solvents under vacuum, crude compound was obtained quantitatively and was directly reengaged in the next step.

^{1}H NMR (400 MHz, DMSO-d_6): δ (ppm) = 1.37 (s, 3 x CH_3, t-Bu), 1.40 (s, 3 x CH_3, t-Bu), 1.90–2.10 (m, CH_2, Glu-C*H*$_2^{\beta}$), 2.21 (s, CH_3, C*H*$_3$CONH), 2.26–2.33 (t, CH_2, C*H*$_2^{\gamma}$, J = 7.36 Hz), 4.29–4.39 (m, CH_2, Glu-C*H*$^{\alpha}$), 5.98 (s, CH_2, pterin-C*H*$_2$), 8.63 (d, NH, Glu-N*H*, J = 7.85 Hz), 8.72 (s, 1H, triazole-C*H*), 8.99 (s, 1H, pterin-*H*),

^{13}C NMR (400 MHz, DMSO-d_6): δ (ppm) = 23.98 (*C*H$_3$CONH), 25.84 (Glu-*C*H$_2^{\beta}$), 27.63 (3 x *C*H$_3$, t-Bu), 27.71 (3 x *C*H$_3$, t-Bu), 31.28 (Glu-*C*H$_2^{\gamma}$), 51.76 (Glu-*C*H$^{\alpha}$), 52.14 (pterin-*C*H$_2$), 79.75 (C, t-Bu), 80.78 (C, t-Bu), 127.54 (triazole-*C*H), 130.89 (pterin-*C*), 142.37 (triazole-*C*), 147.14 (pterin-*C*), 149.82 (pterin-*CH*), 149.85 (pterin-*C*), 159.74 (Glu-*C*=O), 170.65 (Pterin-*C*=O), 171.50 (Glu-*C*=O), 174.27 (CH$_3$*C*ONH).

Synthesis of (1-((2-amino-4-oxo-3,4-dihydropteridin-6-yl)methyl)-1*H*-1,2,3-triazole-4-carbonyl)-*L*-glutamic acid **FAA**

The compound **6** (101 mg, 0.17 mmol) was dissolved in trifluoroacetic acid 40% in CH_2Cl_2. The mixture was stirred at r.t. for 1 h. After evaporation of the solvents under vacuum, the residue was dissolved in a solution of sodium hydroxide (1 M, 10 mL) and the mixture was stirred at r.t. for 12 h. Then the pH was adjusted to 2 with a concentrated hydrochloride acid aqueous solution. The solvent was evaporated under vacuum and the residue was purified by preparative HPLC using acetonitrile/water (0.1% TFA; 10:90) to 100% acetonitrile gradient in 15 min, followed by isocratic acetonitrile for 10 min. *R*t = 9.36 min. Pure product **7** was isolated as a white powder (271 mg, 96%).

^{1}H NMR (400 MHz, DMSO-d_6): δ (ppm) = 1.90–2.04 (m, CH, C*H*$_2^{\beta}$), 2.04–2.18 (m, CH, C*H*$_2^{\beta}$), 2.31 (t, CH_2, C*H*$_2^{\gamma}$, J = 7.30 Hz), 4.36–4.47 (m, CH, C*H*$^{\alpha}$), 5.87 (s, CH_2, pterin-C*H*$_2$), 7.33 (bs, NH_2, pterin-N*H*$_2$), 8.60 (d, NH, Glu-N*H*), 8.62 (s, CH, triazole-C*H*), 8.80 (s, CH, pterin-*H)*.

^{13}C NMR (400 MHz, DMSO-d_6): δ (ppm) = 27.78 (Glu-*C*H$_2^{\beta}$), 30.26 (Glu-*C*H$_2^{\gamma}$), 51.15 (Glu-*C*H$^{\alpha}$), 52.09 (pterin-*C*H$_2$), 127.30 (triazole-*C*H), 128.46 (pterin-*C*), 142.40 (triazole-*C*), 144.17 (pterin-*C*), 149.04 (pterin-*C*H), 153.88 (pterin-*C*), 155.40 (pterin-*C*), 159.73 (*C*=O), 160.35 (*C*=O), 172.98 (*C*=O), 173.81 (*C*=O).

Synthesis of Pyro-PEG-NHBoc **7**

Compound **7** was synthesized as described in our patent (patent WO/2019/016397). Only purification method was modified. Briefly, pyropheophorbide a (100 mg, 0.19 mmol), *N*-Boc- 2,2′-(ethylenedioxy) diethylamine (46.4 mg, 0.19 mmol), *N*-(3-Dimethylaminopropyl)-*N*′-ethylcarbodiimide hydrochloride (71.7 mg, 0.38 mmol), 4-(Dimethylamino)pyridine (30.5 mg, 0.25 mmol) were dissolved in THF (30 mL). The mixture was stirred at r.t. for 24 h under nitrogen. The solvent was evaporated under vacuum. Crude compound was obtained quantitatively as a greenish solid and was directly reengaged in the next step.

^{1}H NMR (400 MHz, DMSO-d_6): δ (ppm) = −2.19 (s, NH, Pyro(a)-*NH*), 0.00 (s, NH, Pyro(a)-*NH*), 1.34 (s, 3 x CH_3, *HBoc*), 1.54 (t, CH_3, Pyro(a)-*H8*$_2$, J = 7.50 Hz), 1.83 (d, CH_3, Pyro(a)-*H18*$_1$, J = 7.21 Hz), 2.14–2.26 (m, CH_2, Pyro(a)-*H17*$_1$), 2.40–2.52 (m, CH, Pyro(a)-*H17*$_2$), 2.61–2.72 (m, CH, *H17*$_2$), 2.99–3.11 (m, 3 x CH_2, *PEG—H*), 3.18–3.29 (m, CH_2, *PEG—H*), 3.31–3.39 (m, 2 x CH_2, *PEG—H*), 3.39 (s, CH_3, Pyro(a)-*H7*$_1$), 3.42 (s, CH_3, Pyro(a)-*H2*$_1$), 3.48–3.56 (m, CH_2 + CH_3, Pyro(a)-*H8*$_1$ + Pyro(a)-*H12*$_1$), 4.26–4.35 (m, CH, Pyro(a)-*H17*), 4.55–4.64 (q, CH, Pyro(a)-*H18*, J = 2.96 Hz), 5.08 (d, CH, Pyro(a)-*H13*$_2$, J = 19.99 Hz), 5.23 (d, CH, Pyro(a)-*H13*$_2$, J = 19.99 Hz), 6.14 (d, CH, Pyro(a)-*H3*$_2$, J = 11.61 Hz), 6.29 (d, CH, Pyro(a)-*H3*$_2$, J = 17.84 Hz), 6.72 (t, NH, PEG-*NH*, J = 5.12 Hz), 7.92 (t, NH, Boc-*NH*, J = 5.53 Hz), 8.03–8.10 (dd, CH, Pyro(a)-*H3*$_1$, J = 9.81 Hz), 8.84 (s, CH, Pyro(a)-*H20*), 9.17 (s, CH, Pyro(a)-*H5*), 9.40 (s, CH, Pyro(a)-*H10*).

^{13}C NMR (400 MHz, DMSO-d_6): δ (ppm) = 10.62 (Pyro(a)-*C7*$_1$), 11.48 (Pyro(a)-*C12*$_1$), 11.86 (Pyro(a)-*C2*$_1$), 17.30 (Pyro(a)-*C8*$_2$), 18.39 (Pyro(a)-*C8*$_1$), 22.77 (Pyro(a)-*C18*$_1$), 28.11 (3 x *Boc—C*), vers 28.15 (Pyro(a)-*C17*$_1$), 30.10 (Pyro(a)-*C17*$_2$), 32.26 (PEG—*C*), 38.45 (PEG—*C*), 47.47 (Pyro(a)-*C13*$_2$), 49.32 (Pyro(a)-*C18*), 51.20 (Pyro(a)-*C17*), 68.93 (*PEG—C*), 69.06 (*PEG—C*), 69.32 (*PEG—C*), 69.39 (*PEG—C*), 77.47 (*Boc—C*), 93.60 (Pyro(a)-*C20*), 96.21 (Pyro(a)-*C5*), 103.80 (Pyro(a)-*C10*), 105.93 (Pyro(a)-*C15*), 122.56 (Pyro(a)-*C3*$_2$), 127.64 (Pyro(a)-*C12*), 128.91 (Pyro(a)-*C3*$_1$), 129.91 (Pyro(a)-*C13*), 131.50 (Pyro(a)-*C2*), 134.74 (Pyro(a)-*C4*), 134.99 (Pyro(a)-*C7*), 135.63 (Pyro(a)-*C8*), 136.95 (Pyro(a)-*C11*), 140.54 (Pyro(a)-*C1*), 144.39 (Pyro(a)-*C9*), 147.80 (Pyro(a)-*C14*), 149.71 (Pyro(a)-*C3*), 153.78 (Pyro(a)-*C6*), 155.48 (*Boc—C*), 161.43 (Pyro(a)-*C16*), 171.78 (Pyro(a)-*C19*), 172.11 (Pyro(a)-*C17*$_3$), 191.21 (Pyro(a)-*C13*$_1$).

HRMS (ESI+): *m/z* calcd. For $C_{44}H_{56}N_6O_6$ $[M + H]^+$ 765.4334; found 765.4304.

Synthesis of Pyro-PEG-NH_2 **8**

Compound Pyro-PEG-NHBoc **7** was solubilized in trifluoroacetic acid (2 mL). The solution was stirred at r.t. for 2 h under nitrogen. Then, TFA was evaporated under vacuum. The crude compound was obtained quantitatively as a greenish solid and was directly reengaged in the next step.

^{1}H NMR (400 MHz, DMSO-d_6): δ (ppm) = −2.19 (s, NH, Pyro(a)-*NH*), −0.13 (s, NH, Pyro(a)-*NH*), 1.54 (t, CH_3, Pyro(a)-*H8*$_2$, J = 7.46 Hz), 1.80 (d, CH_3, Pyro(a)-*H18*$_1$, J = 7.12 Hz), 2.09–2.21 (m, CH_2, Pyro(a)-*H17*$_1$), 2.37–2.47 (m, CH, Pyro(a)-*H17*$_2$), 2.56–2.68 (m, CH, *H17*$_2$), 2.87–2.91 (q, CH_2, Pyro(a)-*HPEG*), 3.09 (s, CH_3, Pyro(a)- *H7*$_1$), 3.17–3.21 (q, CH_2, Pyro(a)-*HPEG*, J = 5.78 Hz), 3.29–3.36 (m, CH_2, Pyro(a)-*HPEG*), 3.41 (s, CH_3, Pyro(a)- *H2*$_1$), 3.43–3.51 (m, 2 x CH_2, Pyro(a)-*HPEG*), 3.51_3.62 (m, 1 x CH_3 + 2 x CH_2, Pyro(a)- *H12*$_1$ + Pyro(a)-*H8*$_1$ + Pyro(a)-*HPEG*), 4.25–4.32 (m, CH, Pyro(a)-*H17*), 4.54–4.63 (q, CH, Pyro

(a)-*H18*, *J* = 6.55 Hz), 5.09 (d, CH, Pyro(a)-*H13*$_2$, *J* = 20.01 Hz), 5.24 (d, CH, Pyro(a)-*H13*$_2$, *J* = 19.95 Hz), 6.17 (d, CH, Pyro(a)-*H3*$_2$, *J* = 11.64 Hz), 6.32 (d, CH, Pyro(a)-*H3*$_2$, *J* = 17.96 Hz), 8.03–8.20 (dd, CH + NH + NH_2, Pyro(a)-*H3*$_1$ + PEG-*NH* + PEG-*NH*$_2$), 8.90 (s, 1H, Pyro(a)-*H20*), 9.30 (s, 1H, Pyro(a)-*H5*), 9.58 (s, 1H, Pyro(a)-*H10*).

^{13}C NMR (400 MHz, DMSO-d_6): δ (ppm) = 11.24 (Pyro(a)-*C7*$_1$), 12.13 (Pyro(a)-*C12*$_1$), 12.48 (Pyro(a)-*C2*$_1$), 17.81 (Pyro(a)-*C8*$_2$), 19.00 (Pyro(a)-*C8*$_1$), 23.34 (Pyro(a)-*C18*$_1$), 29.41 (Pyro(a)-*C17*$_1$), 30.70 (Pyro(a)-*C17*$_2$), 32.82 (PEG—*C*), 38.87 (PEG—*C*), 48.06 (Pyro(a)-*C13*$_2$), 49.89 (Pyro(a)-*C18*), 51.81 (Pyro(a)-*C17*), 66.54 (*PEG*—*C*), 69.07 (*PEG*—*C*), 69.34 (*PEG*—*C*), 69.57 (*PEG*—*C*), 94.64 (Pyro(a)-*C20*), 96.76 (Pyro(a)-*C5*), 104.53 (Pyro(a)-*C10*), 106.85 (Pyro(a)-*C15*), 122.93 (Pyro(a)-*C3*$_2$), 128.31 (Pyro(a)-*C12*), 128.79 (Pyro(a)-*C3*$_1$), 130.18 (Pyro(a)-*C13*), 131.88 (Pyro(a)-*C2*), 135.06 (Pyro(a)-*C4*), 135.29 (Pyro(a)-*C7*), 135.62 (Pyro(a)-*C8*), 137.17 (Pyro(a)-*C11*), 140.80 (Pyro(a)-*C1*), 144.48 (Pyro(a)-*C9*), 148.21 (Pyro(a)-*C3*), 162.51 (Pyro(a)-*C16*), 171.93 (Pyro(a)-*C19*), 172.96 (Pyro(a)-*C*=*O*), 195.77 (Pyro(a)-*C13*$_1$).

Synthesis of **PS^{FAA}**

Compound **FAA** (24.5 mg, 0.06 mmol) and N,N′-Dicyclohexylcarbodiimide (46.6 mg, 0.22 mmol) were solubilized in a mixture of DMSO: pyridine (4.5: 2 mL). The mixture was stirred at r.t. for 2 h under nitrogen. Then, compound **8** (30 mg, 0.05 mmol) was added and the reaction mixture was stirred at r.t. for 24 h. Then, the solution was slowly poured into vigorously stirred cold diethyl ether (15 mL). By centrifugation, the precipitate obtained was collected and washed with diethyl ether (50 mL). The compound **PS^{FAA}** was obtained as blue powder (30.5 mg, 64%).

^{1}H NMR (400 MHz, DMSO-d_6): δ (ppm) = −1.97 (s, N*H*, Pyro(a)), 0.24 (s, N*H*, Pyro(a)), 1.59–1.66 (t, CH_3, Pyro(a)-*H8*$_2$, *J* = 7.13 Hz), 1.67–1.76 (m, 1H, Glu-CH_2^{β}), 1.77 (d, CH_3, Pyro(a)-*H18*$_1$, *J* = 7.08 Hz), 1.91–2.03 (m, CH_2, Pyro(a)-*H17*$_1$), 2.04–2.10 (m, 3H, Glu-CH_2^{β}, Glu-CH_2^{γ}), 2.27–2.35 (t, CH_2, Pyro(a)-*H17*$_2$, *J* = 7.21 Hz), 3.11–3.18 (m, 2 x CH_2, Pyro(a)-*HPEG*), 3.21 (s, CH_3, Pyro(a)- *H7*$_1$), 3.43 (s, CH_3, Pyro(a)- *H2*$_1$), 3.50 (m, 4 x CH_2, Pyro(a)-*HPEG*), 3.60 (s, CH_3, Pyro(a)- *H12*$_1$), 3.66–3.74 (q, CH_2, Pyro(a)-*H8*$_1$, *J* = 7.19 Hz), 4.27–4.29 (m, CH, Pyro(a)-*H17*), 4.37–4.49 (m, CH, Glu-CH^{α}), 4.52–4.61 (q, CH, Pyro(a)-*H18*, *J* = 6.88 Hz), 5.12 (d, CH, Pyro(a)- *H13*$_2$, *J* = 20.09 Hz), 5.23 (d, CH, Pyro(a)- *H13*$_2$, *J* = 20.14 Hz), 5.84 (s, CH_2, pterin-CH_2), 6.18 (d, CH, Pyro(a)-*H3*$_2$, *J* = 11.67 Hz), 6.37 (d, CH, Pyro(a)-*H3*$_2$, *J* = 17.87 Hz), 8.16–8.24 (m, CH, Pyro(a)-*H3*$_1$), 8.67 (s, CH, triazole-C*H*), 8.76 (s, CH, pterin-*H7*), 8.89 (s, CH, Pyro(a)-*H20*), 9.43 (s, CH, Pyro(a)-*H5*), 9.70 (s, CH, Pyro(a)-*H10*).

^{13}C NMR (400 MHz, DMSO-d_6): δ (ppm) = 10.89 (Pyro(a)-*C7*$_1$), 11.66 (Pyro(a)-*C12*$_1$), 11.98 (Pyro(a)-*C2*$_1$), 17.46 (Pyro(a)-*C8*$_2$), 18.62 (Pyro(a)-*C8*$_1$), 22.84 (Pyro(a)-*C18*$_1$), 22.84 (Pyro(a)-*C18*$_1$), 25.44 (Glu-C$^{\beta}$), 25.83 (Pyro(a)-*C17*$_1$), 30.12 (Glu-C$^{\gamma}$), 30.28 (Pyro(a)-*C17*$_2$), 38.43 (PEG—*C*), 38.52 (PEG—*C*), 47.53 (Pyro(a)-*C13*$_2$), 49.36 (Pyro(a)-*C18*), 51.17 (Glu-C*H*$^{\alpha}$), 51.22 (Pyro(a)-*C17*), 52.12 (Pterin-CH_2), 68.78 (PEG—*C*), 68.96 (PEG—*C*), 69.03 (PEG—*C*), 69.37 (PEG—*C*), 93.87 (Pyro(a)-*C20*), 96.55 (Pyro(a)-*C5*), 104.31 (Pyro(a)-*C10*), 106.15 (Pyro(a)-*C15*), 122.93 (Pyro(a)-*C3*$_2$), 127.23 (triazole-*C*H), 128.08 (Pyro(a)-*C12*), 128.44 (Pterin-*C*), 129.08 (Pyro(a)-*C3*$_1$), 130.16 (Pyro(a)-*C13*), 131.79 (Pyro(a)-*C2*), 135.05 (Pyro(a)-*C4*), 135.25 (Pyro(a)-*C7*), 136.08 (Pyro(a)-*C8*), 137.21 (Pyro(a)-*C11*), 140.72 (Pyro(a)-*C1*), 142.39 (triazole-*C*), 143.48 (pterin-*C*), 144.84 (Pyro(a)-*C9*), 147.97 (Pyro(a)-*C14*), 149.21 (Pterin-*C*H), 150.04 (Pyro(a)-*C6*), 154.12 (Pterin-*C*), 154.25 (Pyro(a)-*C16*), 158.44 (Pterin-*C*), 159.60 (C=O), 159.70 (C=O), 161.70 (Pyro(a)-*C19*), 171.82 (C=O), 171.42 (C=O), 172.98 (C=O), 173.81 (C=O), 195.37 (Pyro(a)-*C13*$_1$).

HRMS (ESI+): *m/z* calcd. For $C_{54}H_{62}N_{15}O_9$ $[M + H]^+$ 1064.4855; found 1064.4406.

3. Results

3.1. Molecular docking

The molecular docking analysis of FA and FAA ligands confirmed that both ligands docked at the same active side, showing that FAA and FA have a similar affinity towards the FRα binding pocket. However, a difference in the free energy of binding (FEB) of the ligands with FRα is observed with a more negative energy for FA (−10.37 kcal/mol for FA *vs.* -8.34 kcal/mol for FAA). These data indicate that the interaction of FA with FRα is more favorable than FAA. FA established multiple H-bonds with the receptor (ASP 81, TYR 60, ARG 103, HIS 135, GLY 137) (Fig. 1) that help to stabilize the interaction, and the presence of pteroate moiety (pteridine and *p*-aminobenzoic acid) improves the binding stability *via* π-πstacking interaction (TYR 85, TRP 171, TYR 60, TRP 102) (Fig. 1) [33]. FAA on the other hand gave fewer H-bonds with the receptor (LYS 19, TYR 60, ARG 103, and SER 174) (Fig. 1) than FA. The aromatic moiety in the FAA structure consists of pteridine and triazole ring, as the modification of FA into FAA has led to the replacement of *p*-aminobenzoic acid (PABA) by a triazole ring. It was found that only the pteridine moiety contributes to the formation of π-π stacking interaction with the non-polar amino acids of the receptor (TYR 85 and TRP 171) (Fig. 1). The absence of PABA in FAA has reduced both bonding-bonds and π-π stacking interactions with the receptor, which subsequently affect the FEB of FAA with FRα.

However, the presence of a flexible PEG spacer and a large PS structure introduces the possibility of PS^{FAA} ligands exhibiting distinct interactions from FA and FAA, given their nearly double flexible torsion energy (+7.16 kcal/mol for PS^{FAA}, +3.28 kcal/mol for FAA, and + 4.18 kcal/mol for FA). Therefore, to ensure that coupling FAA to pyro does not hinder its ability to bind to the Frα receptor, we conducted an extensive molecular docking analysis of PS^{FAA}. The analysis reveals that PS^{FAA} has a less negatively charge (−6.80 kcal/mol) compared to FAA and FA, indicating its lower favorability in comparison. However, despite this, PS^{FAA} surprisingly forms an equal number of hydrogen bonds as FAA at five different sites (4 hydrogen bond sites with the pteridine ring against ASP 81, THR 82, HID 135, and 1 hydrogen bond with the PS ring against SER 101), along with a higher number of π-π stacking interactions (6 π-π stacking sites at the pteridine group against TYR 85, TRP 171, and PHE 62, and 2 π-π stacking sites at the PS ring against TRP 102) (Fig. 2). Additionally, it exhibits additional interactions such as a π-lone pair interaction at the α-tail of glutamic acid, a π-donor hydrogen bond at the triazole ring against TYR 60, and two alkyl hydrophobic interactions at the PS region against LYS 104 and LYS 19 (Fig. 2). We also found out that the PEG spacer neither form any interaction or repulsion towards any amino acid of FRα. These findings elucidate how PS^{FAA} can accommodate the high flexible torsion energy while binding to the binding sites of FRα and did not hinder the binding of the pteridine and triazole region with the presence of the PEG spacer. In terms of inhibition constant, K_i, it is predicted that PS^{FAA} has higher value (K_i PS^{FAA} = 10.2 μM) than FA and FAA (K_i FA = 4.84 nM and K_i FAA = 70.78 nM) towards FRα validating that the selectivity of PS^{FAA} is in a good affinity range towards FRα but less potent as FA and FAA. As compared to RFC (control), PS^{FAA} has a very high K_i value which indicates its less affinity towards RFC (K_i PS^{FAA} at RFC = 941.602 mM) as compared towards FRα.

From a three-dimensional (3D) standpoint, the position of the pteridine ring of PS^{FAA} is observed to be slightly shifted away from the targeted position of FA and FAA due to the presence of PS at the end tail (Fig. 3). This explains why the hydrogen bond formed at the pteridine ring of PS^{FAA} differs from that of FAA within the close proximity area, where weak Van Der Waals forces previously existed and now shift to hydrogen bond formation. This shift also facilitates the triazole ring's interaction with the nearest amino acid by forming a π-donor hydrogen bond at the triazole ring against TYR 60 (Fig. 2), thereby enhancing the binding interaction and reducing the FEB. Although this shift also positions PS^{FAA}'s glutamic acid tail further away from THR 60 and LYS 19 (Fig. 2), and the presence of PS also straightens the bond angle between the glutamic acid tail and the spacer chain compared to folded glutamic acid alone in FAA (Fig. 3), PS^{FAA} is able to overcome this missing interaction issue by forming interactions with TRP 140 (Fig. 2). Through an extensive molecular docking simulation, we identified the crucial

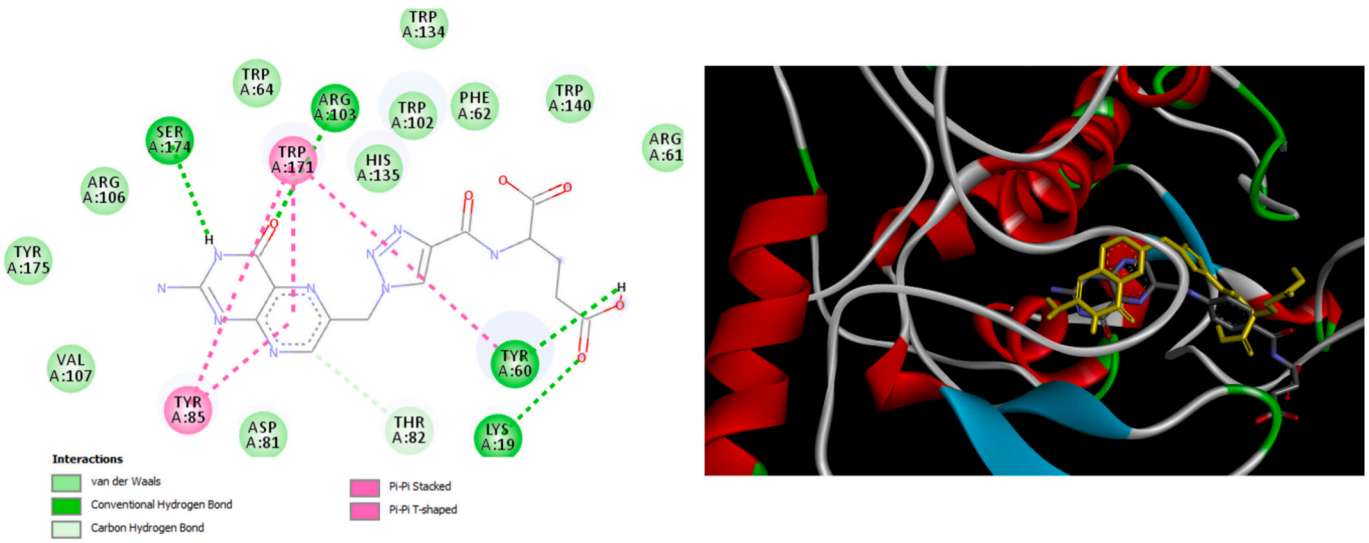

Fig. 1. (Left) 2D interaction analysis of docked *FAA* with FRα binding site. (Right) Superposition of docked models of FA (blue/grey) and *FAA* (yellow). (For interpretation of the references to colour in this figure legend, the reader is referred to the web version of this article.)

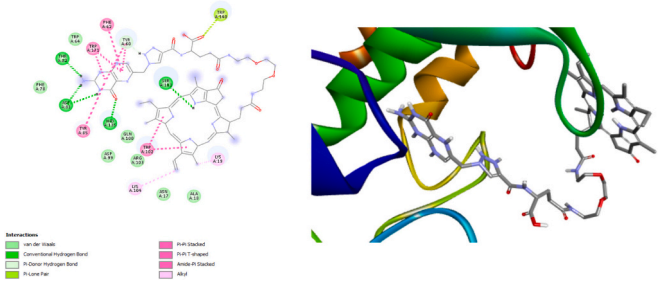

Fig. 2. (Left) 2D interaction analysis of docked PS^{FAA} with FRα binding site.

role of SER 101 in stabilizing the binding of the PS of PS^{FAA} to the binding sites with other complementary amino acids of TRP 102, LYS 104, and LYS 19 (Fig. 3).

3.2. Synthesis

Based on molecular docking studies, we synthesized a new FAA that would be more stable than FA while still having high affinity for FRα.

Thanks to our undisputed expertise in the field of organic chemistry, we have made several modifications of FA at the two labile linkages by changing these labile bonds and the aromatic cycle with the aim to enhance the H-bond network between the pterin moiety and the active pocket of the FRα, but also to stabilize the two π-π stacking interactions between PABA ring and some residues (Fig. 1).

Herein, we designed a new PS for an efficient targeted-PDT treatment of EOC. The designed PS, named PS^{FAA}, is based on three unities: (1) Pyro-*a* as a PS, which could be illuminated in the red region (QI = 668 nm), (2) a PEG spacer, 2,2′-(ethylenedioxy)-bis-ethylamine, to improve water solubility and biocompatibility, and (3) a newly synthesized FAA, to overcome the photostability problem of FA and to target FRα (Schemes 1 and 2).

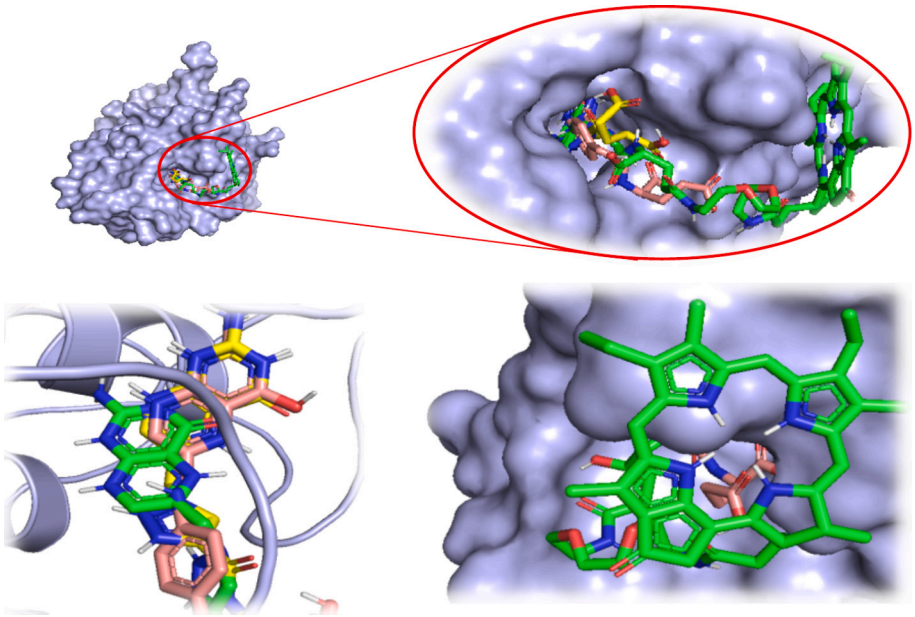

Fig. 3. 3-D interaction analysis of docked PS^{FAA} with FRα binding site. Superposition of docked models of FA (pink carbon chain), FAA (yellow carbon chain) and PS^{FAA} (green carbon chain). (For interpretation of the references to colour in this figure legend, the reader is referred to the web version of this article.)

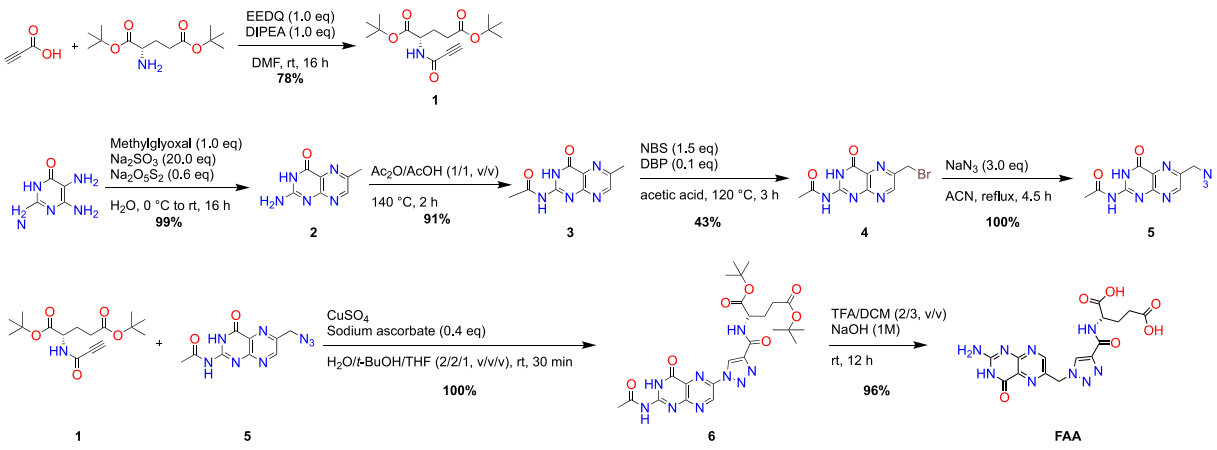

Scheme 1. Chemical synthesis of folic acid analog FAA.

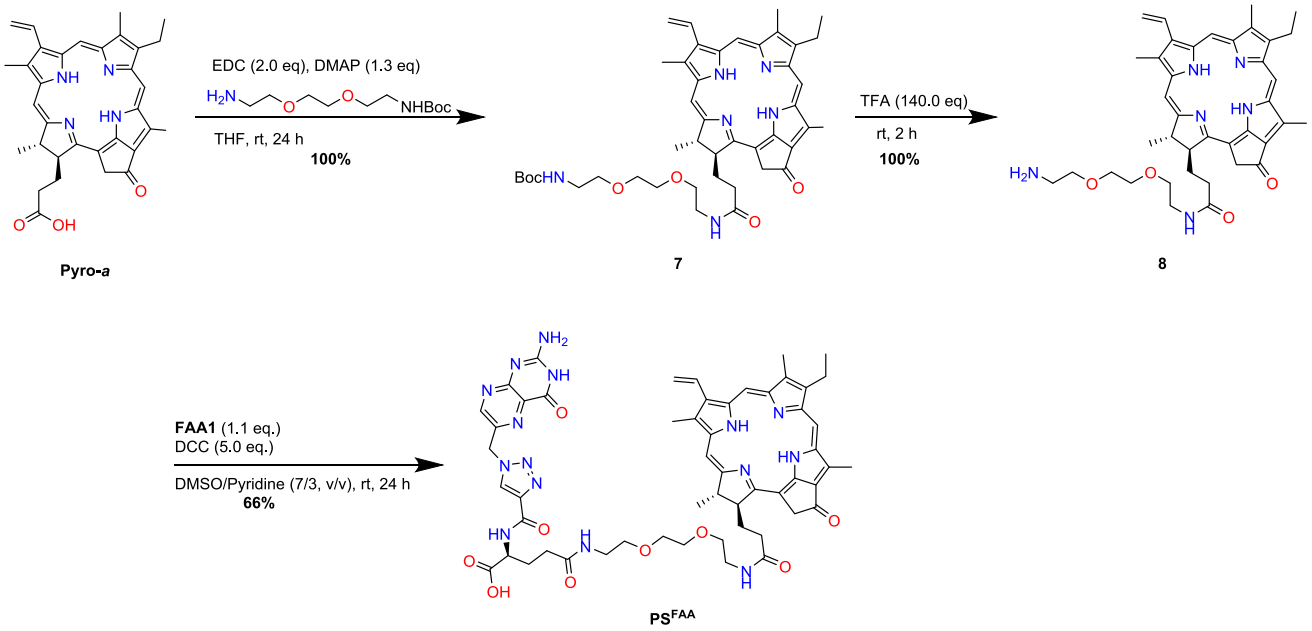

Scheme 2. Chemical synthesis of PS^{FAA}.

PS^{FAA} was prepared in 10 steps for a 19% overall yield. Its synthesis consists of synthesizing of FAA in 7 steps followed by the successive conjugation of the PEG spacer and Pyro-*a* using coupling peptide conditions. The synthesis of FAA involved the use of a Copper-catalyzed azide–alkyne cycloaddition (CuAAC) click chemistry reaction and required the synthesis of the glutamic acid part with an alkyne group and the pterin derivative with an azide group.

First, the alkyne functionalized glutamic acid **1** was obtained in 78% yield (Scheme 1) after a peptide coupling reaction between the free amino group of the di-*tert*-butyl *L*-glutamate with the carboxylic acid function of propiolic acid using EEDQ and DIPEA in DMF.

Second, the synthesis of the azide functionalized pterin **5** was performed in 4 steps (Scheme 1) and started with the condensation of 2,5,6-triaminopyrimidin-4(3*H*)-one with methyl glyoxal using sodium sulfate and sodium metabisulfite which led to the obtention of compound **2**. The free amino group of **2** was then acetyl protected by using a mixture of acetic acid and acetic anhydride to give compound **3**. After that, NBS and dibenzoyl peroxide in acetic acid were used for brominating the methyl group of **3**, and compound **4** was afforded in 43% yield after purification. Finally, the azide substitution of the bromide group of **4** was carried out to yield the azide functionalized pterin **5** quantitatively.

The CuAAC click chemistry reaction between **1** and **5** was performed quantitatively with copper sulfate and sodium ascorbate in a mixture of water and THF to furnish compound **6**. Finally, deprotection of the acetyl and tert-butyl protected groups with a solution of TFA (40% in DCM) followed by a solution of NaOH 1 M, led to the obtention of the desired FAA in 96% yield after purification.

The synthesis of PS^{FAA} from FAA required 3 steps. Firstly, the carboxylic acid handle of Pyro-*a* was attached to a PEG spacer (*N*-Boc- 2,2′-(ethylenedioxy)diethylamine) under coupling conditions (EDC and DMAP in THF) and afforded *N*-Boc-terminated PEG-Pyro-*a* **7** in quantitative yield (Scheme 2). After quantitative Boc deprotection of **7** with TFA (yielding **8**), the resulting free amino group was attached to the carboxylic acid handles of FAA under peptide coupling conditions (DCC in DMSO/pyridine). The desired PS^{FAA} was then obtained as black solid in 66% yield (HPLC purity of 98%), after reprecipitation in cold diethyl ether (Scheme 2). The obtention of PS^{FAA} was confirmed by LC-MS and NMR analysis.

3.3. Photophysical properties

The photophysical properties of FAA and PS^{FAA}, but also FA and Pyro-*a* (as references), were evaluated. Pyro-*a* was used for comparison with PS^{FAA} to evaluate the effect of the FAA coupling on the

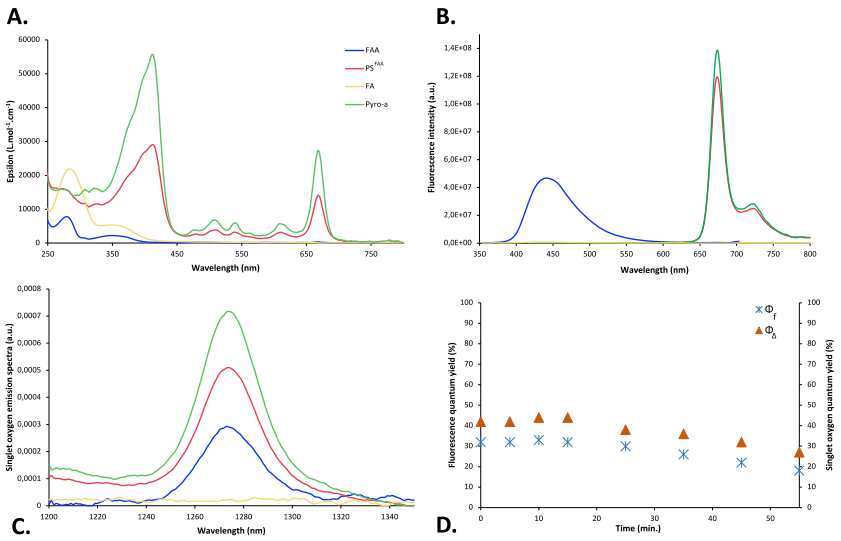

E.

		Pyro-*a*	PS^{FAA}
ε (L.mol-1.cm-1)	Soret band	54406	29827
	Q_{IV}	6649	4111
	Q_{III}	6120	3442
	Q_{II}	5516	3291
	Q_I	27656	14455
Φ_f (%)		39	32
Φ_Δ (%)		53	42
τ_f (ns)		6,9	6,9
τ_Δ (ms)		14,1	12,7

		FAA	FA
ε (L.mol-1.cm-1)	π-π*	7563	16814
	n-π*	2163	5381
Φ_f (%)		23	0
Φ_Δ (%)		11	0

Fig. 4. Photophysical properties of FA, FAA, PS^{FAA} and Pyro-a in EtOH: (A) UV–Visible absorption spectra, (B) Fluorescence emission spectra (λ_{exc} = 410 nm for Pyro-a and PS^{FAA} and λ_{exc} = 349 nm for FA and FAA), (C) $^1O_2$ emission spectra (λ_{exc} = 410 nm for Pyro-a and PS^{FAA} and λ_{exc} = 349 nm for FA and FAA). (D) Photobleaching study. Evolution of the Φ_f and Φ_Δ quantum yields of PS^{FAA} under one-hour light irradiation (668 nm, 10 mW.cm^{-2}). (E) Absorption coefficient, Φ_f, Φ_Δ, τ_f and τ_Δ.

photophysical properties of Pyro-*a*. FA was used for comparison with the new FAA to estimate the chemical modification effect on the photophysical FA. The photophysical studies were evaluated in EtOH due to solubility requirements. In the design of PS^{FAA}, a spacer was introduced between FAA and pyro-a in order to avoid steric hindrance, which could adversely affect the photophysical properties of the pyro-a and the affinity of FAA for the receptor.

The absorption spectra of PS^{FAA} exhibited characteristic bands of porphyrins, as Pyro-*a* alone. We can observe the Soret band at 410 nm and four Q bands (QI, QII, QIII, and QIV) at 668 nm, 612 nm, 540 nm, and 509 nm, respectively. An additional larger shoulder was noticed at the beginning of the Soret band of PS^{FAA}, attributed to the presence of FAA.

Regarding the absorption spectra of FAA and FA alone, identical bands were observed at 278 nm and 349 nm, corresponding to the π-π* and n-π* electronic transitions in the molecular structure of FAA and FA molecules.

To determine the molar extinction coefficient (ε), the absorption spectra of each compound were measured at different concentrations. Although the ε value for the Soret and QI bands decreased after coupling Pyro-*a* with a PEG spacer and FAA, the molar extinction coefficient of PS^{FAA} remained sufficient for its application in PDT. A decrease in the ε value was also observed for both the π-π* and n-π* bands of FAA compared to FA, which can be attributed to the loss of aromaticity caused by replacing the benzoic part of FA with a triazole function (Fig. 4).

Solutions of Pyro-*a*, PS^{FAA}, FAA and FA were prepared at a concentration allowing an absorbance of about 0.2. Fluorescence spectra were recorded with an excitation wavelength of 410 nm for PS^{FAA} and 349 nm for FAA and FA (Fig. 4). Pyro-*a* was used as a reference for calculating Φ_F and Φ_Δ. Fluorescence emission spectra of FAA demonstrate one emission band at 441 nm. Unlike FA, which exhibited no fluorescence or singlet oxygen ($^1O_2$) production, FAA displayed fluorescence with Φ_F = 0.23 and produced $^1O_2$ species with Φ_Δ = 0.11. Fluorescence emission spectra of PS^{FAA} is typical of porphyrin derivatives, with two emission bands at 674 nm and 722 nm. PS^{FAA} demonstrated photophysical properties similar to Pyro-*a*, with Φ_F and Φ_Δ values of 0.32 and 0.42 compared to Φ_F and Φ_Δ values of 0.39 and 0.53 for Pyro-*a*, respectively, indicating that the coupling of FAA does not influence drastically the photophysical characteristics of Pyro-*a*. Furthermore, lifetime of fluorescence (τ_f) and lifetime of singlet oxygen (τ_Δ) of Pyro-*a* remained almost the same in PS^{FAA} with τ_f = 6.9 ns and τ_Δ = 12.7 μs. The coupling of a targeting unit to a PS can influence or not the photophysical characteristics of the PS. Indeed, we showed that the coupling of KDKPPR peptide or alcoxyamine and KDKPPR peptide to Pyro-*a* [34] induced a decrease of the molar absorption coefficient but no change in Φ_f and Φ_Δ. In a scientific review published in 2015 by A. Stallivieri et al. [35], we showed that depending on the type of PS coupled to FA, photophysical properties changed or not. However, these changes did not compromise the overall capability of the compound to induce effective PDT.

These results illustrate the potential of PS^{FAA} for an effective application in PDT.

3.4. Photobleaching studies

Photobleaching studies were conducted to investigate the light illumination effect over the time on the photophysical properties of PS^{FAA} in EtOH (668 nm, 10 mW.cm^{-2}) (Fig. 4). Φ_F and Φ_Δ were measured every 5 min during the first 25 min of light illumination and then every 10 min thereafter until an hour of illumination. As we can see, Φ_F and Φ_Δ remain quite stable throughout the illumination period and are still high after one hour (Φ_F = 0.26 and Φ_Δ = 0.36). This long-time stability of photophysical properties is promising for the use of PS^{FAA} as targeted PDT agent, since the PDT treatment duration should not exceed 30 min clinically.

3.5. FRα expression and ability of PS^{FAA} to target FRα

3.5.1. FRα expression in SKOV3, OVCAR3 and HT1080 cells

In order to evaluate the biological properties of PS^{FAA}, we used two EOC cell lines overexpressing FRα (OVCAR3 and SKOV3) and one fibrosarcoma cell line underexpressing FRα (HT1080) as a negative control.

Transcript analysis showed that ovarian tumor cell lines (SKOV3, OVCAR3) expressed the FRα isoform as expected. However, there was no significant difference between OVCAR3 and SKOV3 cell lines (p = 0.1266). We noticed that HT1080 cell line under-expressed the transcript of FRα compared to OVCAR3 (p = 0.0013) and SKOV3 (p = 0.0003) cell lines (Fig. 5A.1). Concerning the total protein expression analysis by western blot, we observed a stronger expression for the SKOV3 cell line followed by OVCAR3 and finally HT1080 (Fig. 5A.2). However, this observation was not correlated with membrane protein

expression level analyzed by flux cytometry as we noticed a higher expression for OVCAR3 than SKOV3. Finally and once again no expression was detected for HT1080 (Fig. 5A.3). These results confirmed us the interest of using this cell line as a negative control of FRα expression in order to evaluate the PDT selectivity of PS^{FAA} to FRα.

3.5.2. *FRα-targeting of PS^{FAA}*

Subsequently, we evaluated the targeting ability of PS^{FAA} to FRα by a competitive experiment with free FA (Fig. 5B.) For the OVCAR3 cell line, we noticed an early and significant decrease of the fluorescence intensity from 2 h of incubation ($p = 0.0421$). This intensity continued to decrease with the incubation time. For the SKOV3 cell line, the decrease in the fluorescence intensity became significant ($p = 0.0018$) from 6 h of incubation and continued to regress over time. For HT1080 cell line, we noticed that the fluorescence intensity in the HT1080 + PS^{FAA} condition was two times lower than the one observed with OVCAR3 and SKOV3 (20 for HT1080 *vs.* 40 for OVCAR3 and SKOV3). Furthermore, this fluorescence did not decrease over time. These results highlight the

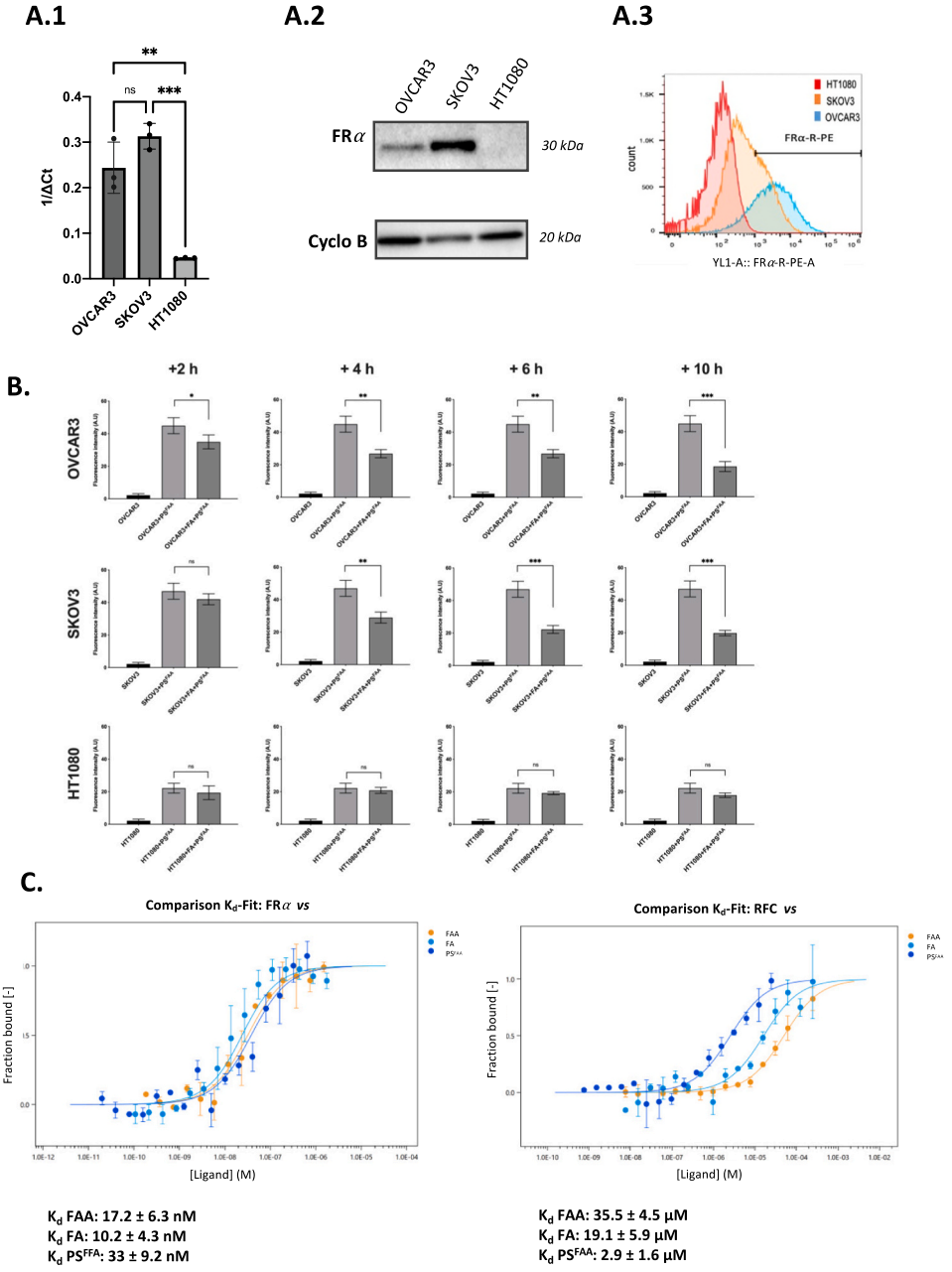

Fig. 5. FRα expression and ability to target FRα. (A) FRα expression by ovarian tumor cell lines (OVCAR3 and SKOV3) and fibrosarcoma cell line (HT1080): (A.1) FRα gene expression by RTqPCR analysis. ΔCt = Ct target gene – Ct HKG. Results are represented as mean ± SD of 3 independent experiments and expressed as 1/ΔCt. One-way ANOVA statistical test is performed, all quoted *p*-values are two-sided with $*p < 0.05$, $**p < 0.01$ and $***p < 0.001$. (A.2) Representative figure of total protein FRα expression by western blot analysis. (A.3) Membrane protein FRα expression by flow cytometry analysis. Fluorescence intensity representation by FlowJo Software. (B) PS^{FAA} ability to target FRα in ovarian tumor cell lines (OVCAR3 and SKOV3) and fibrosarcoma cell line (HT1080) over time: Results are represented as mean ± SEM of 3 independent experiments and expressed in fluorescence intensity. One-way ANOVA statistical test is performed, all quoted p-values are two-sided with $*p < 0.05$, $**p < 0.01$ and $***p < 0.001$. (C) Dose-response curves for the binding interaction between PS^{FAA}, FA, FAA and FRα (left) and PS^{FAA}, FA, FAA and RFC (right). All the curves are shown as the fraction bound against ligand concentration to show their similarity, regardless of the variation of the protein under study. Results are represented as mean ± SD of 3 independent experiments.

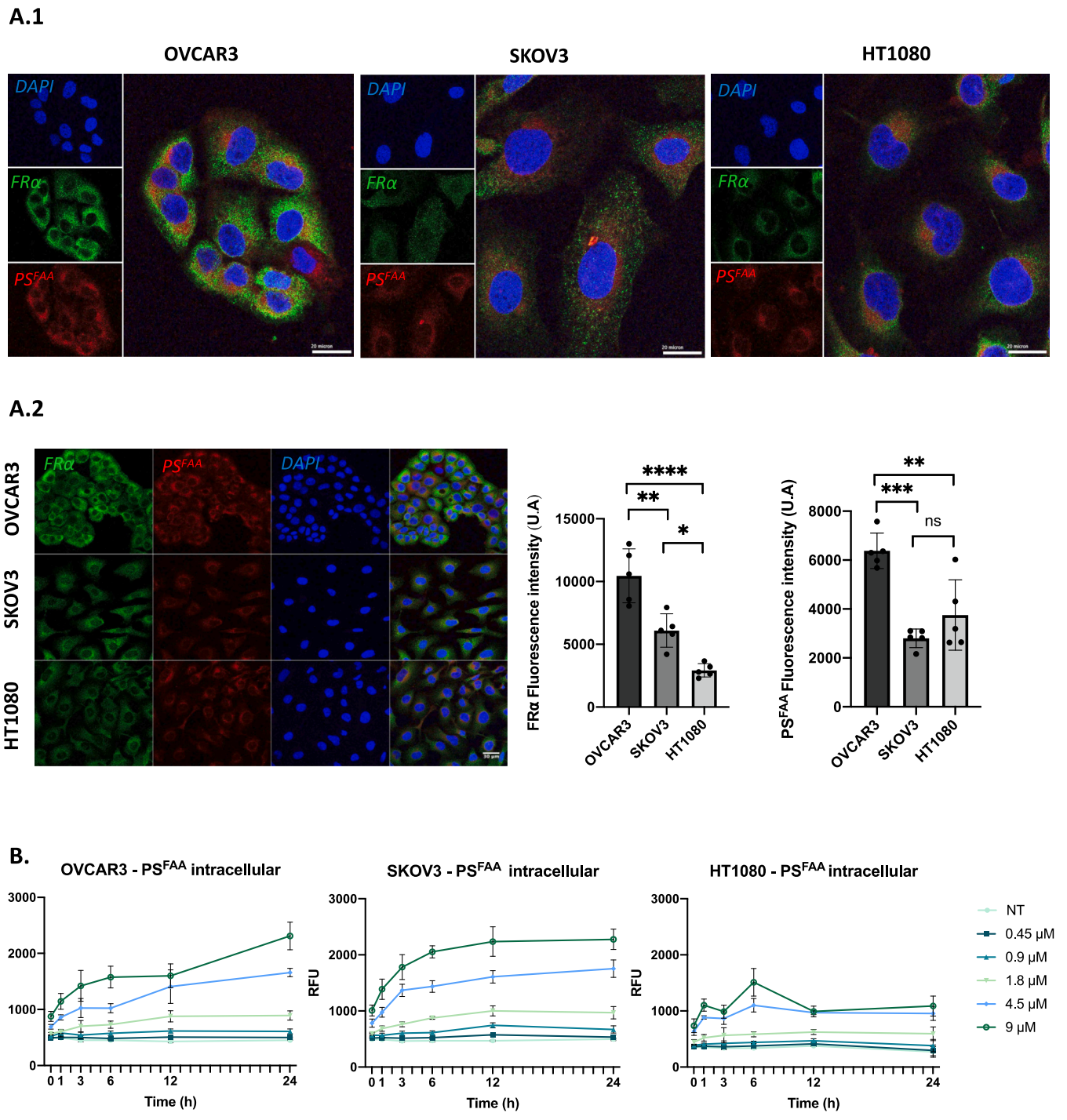

Fig. 6. Effectiveness of the PDT treatment with PS^{FAA} on ovarian tumor cell lines (OVCAR3 and SKOV3) and fibrosarcoma cell line (HT1080). (A) Qualitative and semi-quantitative PS^{FAA} incorporation within ovarian tumor cell lines (OVCAR3 and SKOV3) and fibrosarcoma cell line (HT1080): (A.1) Confocal microscopy-based PS^{FAA} accumulation in OVCAR3, SKOV3 and HT1080 cell lines cultured with 9 µM for 24 h and observed at Gx63 (Confocal Zeiss LSM 710). (A.2) Confocal microscopy-based PS^{FAA} accumulation in OVCAR3, SKOV3 and HT1080 cell lines culture with 9 µM for 24 h observed at Gx40 (Confocal Zeiss LSM 710) in order to semi-quantify FRα expression and PS^{FAA} incorporation. Histograms are represented as mean ± SEM of 5 independent experiments and expressed in fluorescence intensity. One-way ANOVA statistical test is performed, all quoted *p*-values are two-sided with $^{*}p < 0.05$, $^{**}p < 0.01$, $^{***}p < 0.001$ and $^{****}p < 0.0001$.(B) Quantitative PS^{FAA} incorporation within ovarian tumor cell lines (OVCAR3 and SKOV3) and fibrosarcoma cell line (HT1080) over time. Fluorimetry based PS^{FAA} quantification of OVCAR3, SKOV3 and HT1080 cell lines treated by different concentrations (0 to 9 µM) for different incubation periods (0, 1, 3, 6, 12, 24 h). Intracellular levels are measured by cells in fresh media. The values are represented in Relative Fluorescence Unit (RFU) as mean ± SEM of 3 independent experiments.

targeting ability of our PS^{FAA} to FRα, and this with a better selectivity for cell lines overexpressing FRα.

Based on these results, we decided to evaluate the strength of binding between FA, FAA, PS^{FAA} and FRα by determining their dissociation constants (K_d) (Fig. 5C). In order to estimate the targeting selectivity for FRα, we compared these K_d values with those of reduced folate carrier (RFC) which is a ubiquitous carrier of folate. We noticed that FA and FAA present a similar affinity (K_d of 10.2 nM and 17.2 nM, respectively) for FRα suggesting that our new synthetized FAA has an affinity as strong as the natural ligand (FA). Furthermore, the coupling of the FAA to Pyro-*a* in PS^{FAA} slightly decreased the affinity for FRα (K_d of 33 nM) but thus stayed pretty close to the free FAA. Finally, the affinity for RFC looked quite different from FRα since it is in the micromolar range (K_d of 2.9 μM, 19.1 μM, and 35.5 μM for PS^{FAA}, FAA and FA, respectively) compared to nM range of K_d for FRα. These results suggest the high specificity of our new PS^{FAA} to FRα and its low affinity for RFC should limit off target effect.

3.6. Selective incorporation of PS^{FAA} in cells

Visual analysis and semi-quantitative estimation of FRα labeling showed a significant and higher FRα expression in OVCAR3 cell lines compared to SKOV3 ($p = 0.0016$) and HT1080 ($p < 0.0001$) (Fig. 6, A1 and A2). FRα expression in SKOV3 cell line remained higher compared to HT1080 cell line ($p = 0.0144$). Therefore, these results regarding FRα membrane protein expression confirmed those obtained by flow cytometry in Fig. 5A.3. Regarding the incorporation of PS^{FAA}, visual analysis and semi-quantitative estimation showed a major incorporation into OVCAR3 compared to SKOV3 ($p = 0.0028$) and HT1080 ($p = 0.0221$). However, no statistically significant difference was found between SKOV3 and HT1080 cell lines ($p = 0.4953$) (Fig. 6, A.1 and A.2).

Subsequently, we demonstrated the intracellular accumulation of PS^{FAA} in the three cell lines with a quantitative fluorimetry by culturing cells with various concentrations of PS^{FAA} for varying time points (Fig. 6B). About OVCAR3, we observed a continuous increase in the levels of PS^{FAA} fluorescence for the highest concentrations (9 μM and 4.5 μM), from the earliest point to 6 h. This intracellular level seems to stagnate between 6 h and 12 h before increasing again until reaching a peak at 24 h (2300 RFU). Concerning SKOV3 for the highest concentration, the intracellular fluorescence levels keep on increasing until 12 h after which the level is saturated at 2200 RFU. For HT1080, contrary to the other cell lines as previously described, we can notice a slight increase between 0 and 1 h. Then the fluorescence decreases and seems to increase again between 3 and 6 h. But interestingly, after 6 h, the fluorescence starts to decrease especially since the level of intracellular fluorescence is >2 times lower than OVCAR3 and SKOV3 cell lines (1000 RFU).

3.7. PDT efficiency of PS^{FAA}

Before evaluating the PDT efficiency of PS^{FAA}, we evaluated the innocuity of this new molecule in the dark with a cytotoxic assay *via* LDH release. After treated the cells with different concentrations of PS^{FAA} for 24 h, we did not observe any cytotoxicity of PS^{FAA} for OVCAR3 or SKOV3 cell lines compared to the positive control (Triton 100-X) (Fig. 7A). The DMSO, which is the solvent used to solubilize PS^{FAA}, was non-toxic as well.

Subsequently, in order to evaluate the PDT efficacy of PS^{FAA}, cells were treated with different doses in terms of concentration and illumination power (Fig. 7B.). Results showed a dose effect depending on the concentration and light dose for the three cell lines. This dose dependent effect was stronger on the OVCAR3 cell line as the EC_{50} (half maximal efficacy concentration) was 2 times lower no matter the light dose compared to SKOV3 and HT1080 cell lines. However, SKOV3 and

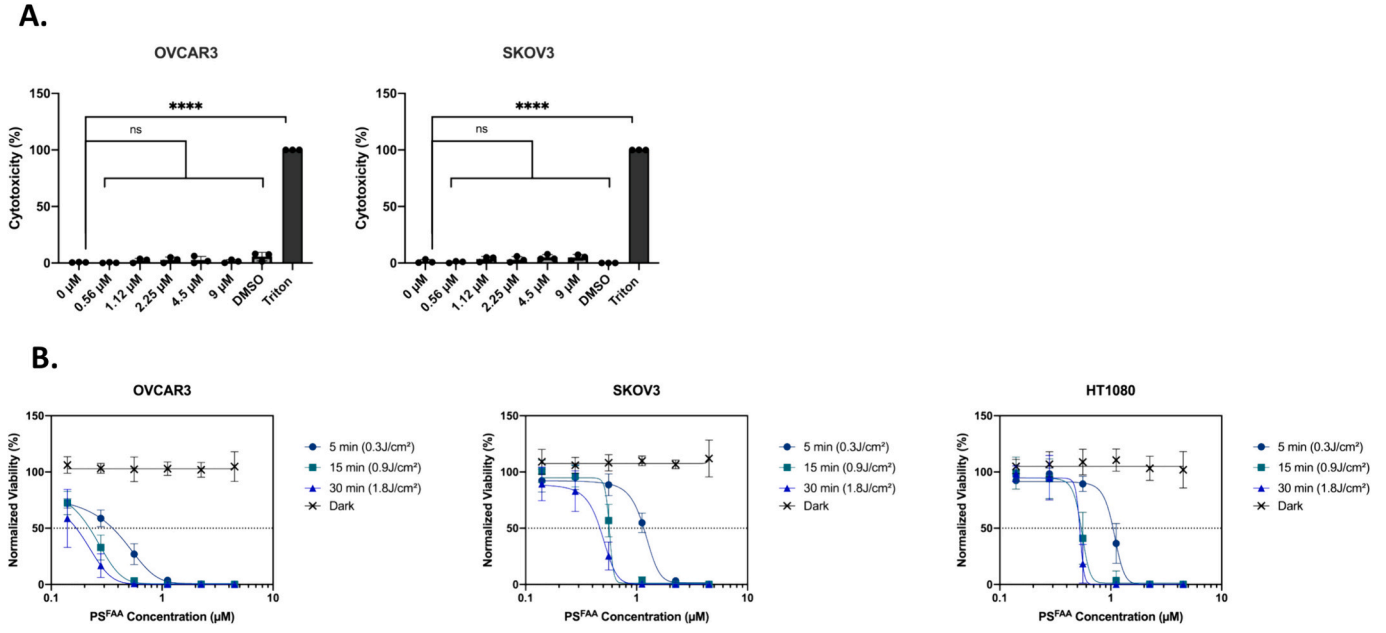

Fig. 7. PDT efficiency of PS^{FAA} on ovarian tumor cell lines (OVCAR3 and SKOV3). (A) Cytotoxicity assay based on Lactate Dehydrogenase Activity on OVCAR3 and SKOV3 cell lines treated with various concentrations of PS^{FAA} (0 to 9 μM) for 24 h. Results are presented as mean ± SEM of 3 independent experiments, expressed in percentage (%) of cytotoxicity and compared to positive control (Triton). One-way ANOVA statistical test are performed, all quoted p-values are two-sided with *p < 0.05, **p < 0.01, ***p < 0.001 and ****p < 0.0001. (B) PDT efficacy of PS^{FAA} on ovarian tumor cell lines (OVCAR3 and SKOV3) and fibrosarcoma cell line (HT1080). Percentage of Normalized Viability for OVCAR3, SKOV3 and HT1080 cell lines 24 h post-treatment incubated with different concentrations of PS^{FAA} (0.14, 0.28, 0.56, 1.12, 2.25 and 4.5 μM) for 24 h. Illumination was performed with laser set at 672 nm, 1 mW/cm^2 and different light doses (0.3, 1.8 and 3.6 J/cm^2). Results are represented as mean ± SEM of 3 independent experiments, expressed in percentage (%) compared to None Treated (NT) cells condition. Half Maximal Effective Concentration (EC_{50}) values are calculated from the viability curves, represented according to the light dose and the different cell lines and showed in Table 2.

HT1080 cell lines presented the same sensitivity to PDT as the dose response curve were similar and the EC_{50} values very close for each light dose (Table 2).

Table 2
Resume of Half Maximum Efficacy Concentration (EC_{50}).

		EC_{50} (μM)		
		OVCAR3	SKOV3	HT1080
Light Dose ($J/cm^{2)}$	0.3 J/cm^2	0.36 μM	1.16 μM	1.05 μM
	0.9 J/cm^2	0.22 μM	0.57 μM	0.54 v
	1.8 J/cm^2	0.17 μM	0.47 μM	0.53 μM

3.8. Impact of the PDT treatment with PS^{FAA} on the microenvironment of OC

Finally, we investigated if PDT could have an impact on the immune system by culturing conditioned supernatants of the SKOV3 and OVCAR3 tumor cells with peripheral blood mononuclear cells (PBMC) (Fig. 8A.). When the PBMC were activated and cultured in the presence of 50% of the media of SKOV3 and OVCAR3 cell cultures subjected to different conditions, the proliferation rate did not change in the PDT condition when compared to NT condition. In fact, the analysis showed that the proliferation was not statistically different between all the conditions. Indeed, the PDT conditioned media did not induce an

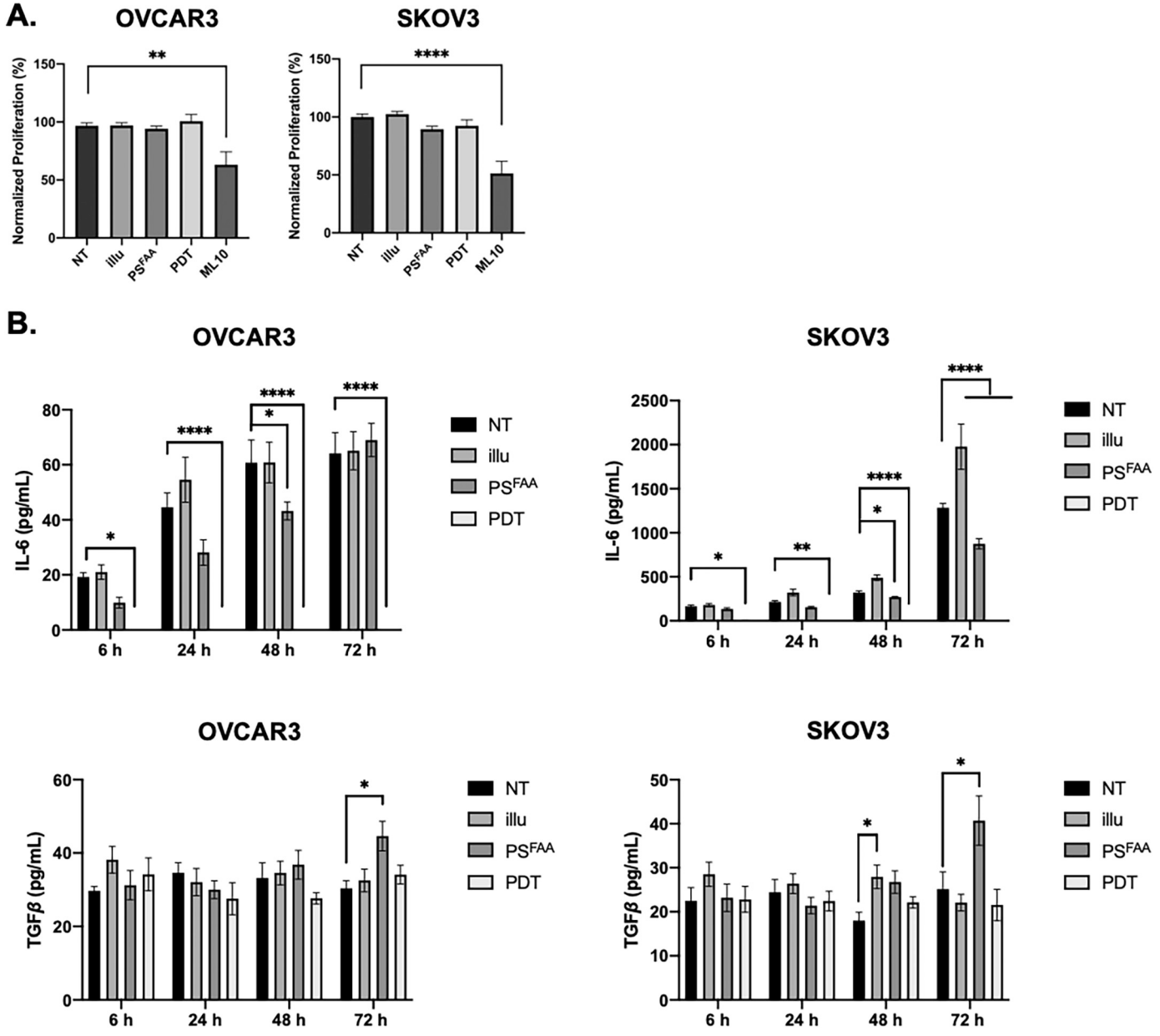

Fig. 8. Impact of the PDT treatment with PS^{FAA} on the microenvironment of OC. (A) Proliferation assay of activated human PBMC culture with conditioned media at 120 h. Results are represented as mean ± SEM of 6 independent experiments, expressed in normalized proliferation compared to NT condition. One-way ANOVA statistical test is performed, all quoted *p*-values are two-sided. NT: non treated, PS^{FAA}: PS^{FAA} only, illu: illumination only, PDT: illumination in the presence of PS^{FAA} and ML10: raw culture media of PBMC. (B) Evaluation of IL-6 and TGFβ secretion upon PDT treatment with PS^{FAA}. ELISA of IL-6 and TGFβ cytokine present in the medium culture under different conditions after being incubated with 9 μM of PS^{FAA} for 24 h and then illuminated with a laser set at 672 nm, 1 mW/cm^2 and 3.6 J/cm^2. Results are represented as mean ± SEM of 3 independent experiments and expressed in pg/mL. Two-way ANOVA statistical test is performed, all quoted p-values are two-sided with $*p < 0.05$, $**p < 0.01$, $***p < 0.001$ and ****p < 0,0001. NT: non treated, PS^{FAA}: PS^{FAA} only, illu: illumination only, PDT: illumination in the presence of PS^{FAA}.

immunosuppressive effect.

Furthermore, in order to evaluate the impact of the PDT treatment with PS^{FAA} on the cytokine secretion by cancer cells, different cytokines were investigated (IL-2, IL-10, TNFα, TGFβ, IL-6 and IFNγ) and represented in Fig. 8B. (only the histograms for the cytokines detected are presented). Analyses of cytokine composition of the reconstituted media recovered from treated cells showed that OVCAR3 and SKOV3 cell lines are able to naturally produce IL-6 and TGFβ. Moreover, SKOV3 secreted more IL-6 than OVCAR3 but no difference was observed between the two cell lines regarding TGFβ secretion (Fig. 8B.).

Concerning IL- 6 secretion, it increased over time in the NT and Illu groups for OVCAR3 and SKOV3. When the cells were in contact with PS^{FAA}, we noticed a slight decrease of the IL-6 secretion 48 h after PDT for the OVCAR3 cell line and 48 h and 72 h post-incubation for the SKOV3 cell line. However, in the PDT condition there was a significant and early decrease (reach 0 pg/mL) in IL-6 from 6 h and which last over time for both cell lines compared to NT. Therefore, the decrease was much larger than that observed in the PS^{FAA} group. Consequently, the results obtained suggest that PDT decreases the production of the pro-inflammatory cytokine IL-6, early and long lasting, by ovarian carcinoma cells.

Concerning TGFβ secretion, no significant change was observed in the PDT condition. These results highlighted that PDT did not affect the production of the immunosuppressive cytokine TGFβ by ovarian carcinoma cells.

4. Discussion

EOC represents the most defying disease among gynecological malignancies. Despite the addition of poly (ADP-ribose) polymerase (PARP) inhibitors (PARPi) and anti-angiogenic agents to conventional therapies, 70% of patients in remission relapse within 18 months [36]. Amate et al., showed in a retrospective study that 75% of relapses in advanced stages occur in the peritoneum due to the persistence of a residual microscopic disease after debulking surgery [37]. One of the symptoms of advanced disease is an abnormal accumulation of fluid in the peritoneal cavity, known as ascites. It contains molecules secreted by EOC cells and the peritoneal microenvironment that can influence proliferation, angiogenesis and dissemination of cancer cells. Among the cytokines found in ascites in significant quantities, we can find IL-6. IL-6 is a pro-inflammatory cytokine, associated with the stage and prognosis of EOC [10]. J. Coward et al., also reported that elevated IL-6 levels are associated with reduced overall survival in EOC patients [73]. IL-6 is secreted autocrine by OC cells and paracrine by cells of the tumor microenvironment, such as fibroblasts and cancer-associated adipocytes. Following secretion, IL-6 binds to its receptor on the cancer cell membrane, and *via* its JAK/STAT signaling pathway, induces different mechanism such as chemotherapy resistance, epithelial-mesenchymal transition (EMT), angiogenesis and metastatic propagation [38,39]. Consequently, there is an emergency to develop new therapeutic strategies able to eradicate mPM and module the pro-inflammatory microenvironment of EOC in order to improve patient prognosis. For such a purpose, the use of therapeutic targeting strategies, such as PDT, would be relevant.

PDT is a complementary approach to classic approaches for the treatment of malignant tumors. However, despite its potential, PDT has faced various limitations that hindered its clinical effectiveness. These challenges include the lack of specificity of the PS for tumor cells, cutaneous photosensitivity, hydrophobicity of the PS, and limited light penetration into target tissues. To overcome these obstacles, significant efforts have been made in recent years to develop new ways of excitation (interstitial PDT (iPDT) [40], two-photons [41], X-ray [42]) and new PSs. Notable advancements include the emergence of tetrapyrrolic-structured PSs, synthetic dyes, functionalized nanoparticles (NPs), and third-generation PSs [43]. In the scope of our study, we have chosen to focus on the use of these third-generation PSs for the specific treatment of PM.

The evolution of PSs towards a third generation has brought significant improvements to overcome major drawbacks observed with second-generation PSs, such as their low solubility in aqueous environments. Third-generation PSs are based on an innovative approach involving the use of NPs that will accumulate into the tumor due to the Enhanced Permeability and Retention (EPR) effect [44] and/or conjugation or vectorization of second-generation PSs with specific targeting molecules. This strategy allows for selective targeting of tumor tissues or neovessels, which represents a considerable advantage compared to non-targeted PSs, as it enhances therapeutic efficacy while reducing adverse effects on surrounding healthy tissues. Additionally, the use of targeted molecules improves the aqueous solubility of the PS, facilitating better PS biodisponibility, thus increasing its concentration and action time in the targeted tissues [45].

FA, also known as vitamin B9, plays a crucial role in various biological processes, including DNA synthesis, cellular metabolism regulation, and cell division [46]. Due to its significance in cellular metabolism, it is commonly used as a targeting agent in various scientific and medical applications. In the context of targeting cancer cells, FA is frequently employed as a cancer cell-targeting agent either by direct coupling to a PS or through the use of a spacer (such as PEG, peptide, or amino acid for example) [35]. FA also finds application in delivering therapeutic substances, such as anticancer agents, by being directly linked to NPs, thus facilitating their targeted delivery to cancer cells [47]. Additionally, FA is used in the development of imaging agents [48,49]. By using FA coupled with specific radio-imaging agents, precise diagnostic images can be obtained, enabling early tumor detection.

The family of folate receptors comprises four distinct isoforms: FRα, FRβ, FRγ, and FRδ, which differ in their expression levels in healthy or cancerous cells. The FRα isoform is a receptor present on the cell surface, anchored by a glycosylphosphatidylinositol membrane [50]. Its expression level is particularly high in numerous epithelial tumors such as ovarian, lung, endometrial, kidney, and breast cancers [51,52]. In contrast, in healthy cells, FRα expression is generally low and limited to a specific localization on the apical/luminal surface of polarized cells, which are not in contact with circulating folate. In the context of EOC, it has been demonstrated that 82% of cancer cells exhibit overexpression of FRα [52], making it a privileged target for our study on the treatment of OC using PDT.

Therefore, we designed and synthesized a new FAA, to enhance FA stability and effectiveness in tumor treatment. It was coupled to Pyro-*a* using a PEG spacer arm.

The use of certain PSs comes with significant drawbacks, including their hydrophobicity and low accumulation in tumor tissues [53]. To overcome these limitations, various approaches can be considered. One of them involves the use of a PEG spacer arm to enhance the PS solubility. Moreover, addition of PEG arm avoids steric hindrance and allows FAA to access FRα. Additionally, the combination of a specific targeting molecule and localized/controlled light illumination will enable targeted accumulation in tumor tissues. Among the promising PS, Pyro-*a* belongs to the chlorin family, which is the reduced form of the porphyrin family, characterized by the reduction of a conjugated double bond in the periphery, leading to structural asymmetry and improvements in its photophysical properties. These enhancements include a red shift in the absorption Q-bands and an increase in the molar extinction coefficient [54,55] compared to PhotoFrin® for example where we can observe an increase of about 25 fold in the molar extinction coefficient and a red shift of about 40 nm in EtOH [31]. An additional advantage of Pyro-*a* is its structure containing a single free carboxylic acid, which facilitates its coupling with a targeting molecule. This characteristic allows obtaining the desired product in a pure form, with sufficient purification through centrifugation. Numerous studies have confirmed the efficacy of Pyro-*a* as a PS for PDT. It has been used in the synthesis of a modular transport system [56] and conjugated with a peptide to target different types of cancer cells that overexpress the $\alpha_v\beta_3$ integrin receptor [55]. Regarding

its photophysical properties, Pyro-*a* exhibits higher Φ_f than some classical porphyrins like tetraphenylporphyrin (TPP). For instance, the Φ_f are 0.31 for Pyro-*a* and 0.11 for TPP in DMF [57]. However, the Φ_Δ of Pyro-*a* is slightly lower than TPP, with $\Phi_\Delta = 0.52$ for Pyro-*a* compared to $\Phi_\Delta = 0.65$ for TPP in DMF [58]. Despite this slight drawback, the potential use of Pyro-*a*n under physiological conditions is higher than that of classical porphyrins due to its improved solubility in polar solvents and the fact that it is a natural PS derived from chlorophyll.

However, stability of FA is of concern due to its decomposition under several parameters, as mentioned earlier [30]. A design of Experiment (DoE) considering various parameters (temperature, presence of light, presence of oxygen, condition time and condition media) was carried out in our laboratory to understand the factors that have the most impact on the degradation of FA.

We designed and synthesized a new FAA, to enhance FA stability and effectiveness in tumor treatment. It was coupled to Pyro-*a* using a PEG spacer arm to afford a new third-generation PS, named PS^{FAA}.

First, the results obtained from molecular docking studies demonstrate differences in interactions between FA, FAA and PS^{FAA} ligands with the FR*α* receptor. Indeed, FA demonstrates a higher free binding energy towards the active site of FRα compared to FAA, due to the presence of several hydrogen bonds and π-π stacked interaction. However, PS^{FAA} is the result of the addition of a PEG spacer arm and a PS, Pyro-*a*, which allows to introduce new interactions with FRα receptor compared to FA and FAA. Even if we can observe a decrease in the free energy binding value of PS^{FAA} for the receptor, this new PS demonstrates an efficient adaptation despite its complex structure, in view of the number of hydrogen bonds and π-π stacked interactions that are maintained. Furthermore, the observation of a slight deviation in the position of the pteridine ring of PS^{FAA} compared to FA and FAA, due to the presence of PS at the tail end, highlights the flexibility of PS^{FAA} in adjusting to the binding sites of FR*α*. This flexibility allows it to compensate for missing interactions and maintain significant interactions with key receptor residues. Additionally, the identification of the crucial role of SER 101 in stabilizing the PS binding with other complementary amino acids underscores the importance of complex interactions in the recognition and binding of more ligands like PS^{FAA} with FR*α*. Finally, we can conclude that the predicted values of the inhibition constant highlight a selective affinity of PS^{FAA} towards FRα.

PS^{FAA} was obtained through a synthesis pathway involving 10 steps and yielding an overall yield of 19%. This synthesis approach allowed us to maintain a certain photophysical efficiency of the final PS^{FAA}, even though some photophysical properties were slightly altered. The coupling of a targeting unit to a PS can influence or not the photophysical characteristics of the PS. Indeed, we showed that the coupling of KDKPPR peptide or alcoxyamine and KDKPPR peptide to Pyro-*a* [34] induced a decrease of the molar absorption coefficient but no change in Φ_f and Φ_Δ. In a scientific review published in 2015 by A. Stallivieri et al. [35], we showed that depending on the type of PS coupled to FA, photophysical properties changed or not. However, these changes did not compromise the overall capability of the compound to induce effective PDT.

The photophysical studies conducted on our new FAA in comparison to FA have revealed surprising results regarding Φ_f and Φ_Δ. Unlike FA, FAA exhibits the ability to emit fluorescence and generate $^1O_2$ when exposed to light. This discovery has sparked significant interest, as it suggests that structural differences between FAA and FA are responsible for these divergent photophysical properties. To elucidate the involved reaction mechanisms and intermediate steps occurring after the molecule absorbs light, flash photolysis studies are being considered.

Furthermore, one of the essential characteristics of PS^{FAA} lies in its photostability during light irradiation, which is crucial for its application in PDT. Our photobleaching studies demonstrated that PS^{FAA} retained its stability with prolonged illumination time up one hour, ensuring its efficacy in PDT treatment. These results are in agreement with photobleaching studies performed on Pyro-*a* based PS already described in the literature [34].

After validating the promising photophysical properties of this new PS^{FAA}, we investigated its biological effect in an *in vitro* model of OC. To demonstrate the PDT efficacy of PS^{FAA}, we used two OC cell lines (OVCAR3 and SKOV3) overexpressing FR*α*.

Subsequently, in order to evaluate the potential of FRα-targeted PS in PDT, we added to our panel of cells, a fibrosarcoma cell line (HT1080) underexpressing FRα [35]. We confirmed the gene and protein expression of FRα in our tumor cell lines. Transcript expression was significantly higher in the OVCAR3 and SKOV3 cell lines compared to HT1080. Concerning membrane protein expression, OVCAR3 expressed more FRα than SKOV3 as it was shown by flow cytometry and immunofluorescence and as it was also described by M. Bagnoli et al. [59]. The absence of FRα expression by the HT1080 cell line confirmed us the interest of using it as a control in order to study the specificity of PS^{FAA} to for FRα targeted PDT.

As mentioned earlier, folate uptake involves several transporters, such as FRα and RFC. Unlike FRα which is a single chain glycosylphosphatidylinositol-anchored membrane protein overexpressed by different epithelial cancer, RFC is an ubiquitously expressed transporter for natural folates and classical antifolates [60]. Therefore, a too high affinity of the PS^{FAA} for RFC could lead to side effects to healthy tissue. That is why, we evaluated the equilibrium dissociation constant (K_d) between the 2 folate receptors (FRα and RFC) with PS^{FAA}, FAA and FA. Furthermore, in order to compare the affinity of the molecules between them, we also determined the K_d between the FRα and FA which was equal to 10.2 nM. This K_d value is quite close to those described in the literature [61–63]. The slight difference in K_d values indicates that the method used to measure the Kd can have an influence on the outcome. With our method, results showed that FA and FAA present a similar affinity for FRα suggesting that our new synthetized FAA has an affinity as strong as the natural ligand. When FAA was coupled to Pyro-*a*, we noticed a slight decrease of the affinity to FRα as we observed with the Ki. Even if, K_d and K_i values of PS^{FAA} towards FR*α* were higher than FAA alone it remains in a very good affinity range. All the more so as we showed that the affinity of PS^{FAA} for RFC was very different since it is in the μM range compared to nM range for FRα. Subsequently, we confirmed the FR*α* targeting of PS^{FAA} through a competitive experiment with FA. The decrease of the fluorescence intensity of the PS^{FAA} as the concentration of FA increases highlighted the preferential FR*α* targeting. Taking together, these results confirmed that our new PS^{FAA} is specific to FRα and its very low affinity for RFC would limit the off-target effect.

Then, we evaluated the ability of the PS^{FAA} to incorporate within the cell lines overexpressing FRα compared to HT1080. Qualitative and semi-quantitative evaluations of the fluorescence showed that after 24 h of incubation, OVCAR3 presented a massive internalization compared to SKOV3 and HT1080. However, when analyzed by a quantitative method such as fluorimetry, the uptake reflected by the RFU was the highest at 24 h for OVCAR3 and SKOV3 compared to HT1080. Once again, these results demonstrated the selective targeting on FRα positive cell lines of our PS^{FAA}. From these results, 24 h of the incubation period was chosen before illuminating the cells to induce a PDT effect.

Before performing PDT, we showed that this PS^{FAA} alone was not cytotoxic in the dark, thus demonstrating its innocuity when it used alone. When cells were illuminated with a laser at 672 nm developed by our team [32], we noticed a dose effect depending on PS^{FAA} concentration and light dose. OVCAR3 cell line appeared to be the most sensitive to the PDT treatment with PS^{FAA}. These results were expected given the high expression of the receptor. On the other hand, no differences between SKOV3 and HT1080 were noticed despite a different expression. This could be explained by the high degree of malignancies of the SKOV3 cell line which has already been described by Kobayashi et al. [64]. In fact, this high invasive tumor cell line releases significantly more exosomes containing proteins involved in processes, such as cell death and survival, cell growth and proliferation, which could explain the resistance of this cell line to the PDT treatment with PS^{FAA}.

Finally, we investigated the potential immunostimulating or immunosuppressive effects of PDT by culturing conditioned supernatants of the SKOV3 and OVCAR3 tumor cells with PBMC with a proliferation assay. In fact, the potential of PDT to induces these effects has already been described in the literature [29,65–68]. We confirmed that PDT does not decrease the proliferation of immune cells. Therefore, the PDT treatment with our PS^{FAA} does not present any immunosuppressive effect contrary to current chemotherapies. Then, we analyzed the secretome of the cancer cells subjected to PDT. Several cytokines were analyzed as IL-6, TGFβ, IFNγ, IL-10 and IL-2. This analysis showed that SKOV3 secreted much more IL-6 than OVCAR3 when cells were not treated. These results have also been observed by Zang et al. [69]. In fact, IL-6 is one of the pivotal immunoregulatory cytokines present in the EOC microenvironment. Its binding to the IL-6 receptor induces signaling pathways involving in proliferation, angiogenesis, and resistance. That's why, high levels of IL-6 have been found in patients with OC and these levels have been shown to correlate with the extent of the disease and poor clinical outcome [73]. Therefore, given their level of malignancy, it is not surprising that SKOV3 secreted high levels of IL-6 and are more resistant to PDT. More interestingly, after PDT, we noticed a significant decrease of the IL-6 secretion in the PDT condition only for both cell lines. These results were also observed in our previous study with our patented PS coupled to FA [28]. Concerning the immunosuppressive cytokine TGFβ, we noticed that both of the tumor cell lines were able to naturally secrete it but we did not observe any changes in the secretion after PDT. We also evaluated the PDT ability of PS^{FAA} to modulate treated tumor cell's secretome by analyzing other cytokines related to development of OC and immunosuppression like IL-10 and TNFα [11,70] but also cytokines related to tumor regression and immunoactivation like IL-2 and IFNγ [71,72]. Unfortunately, we did not detect any secretion of these cytokines in the control condition suggesting, (i) that EOC cell lines are not able to secrete these cytokines and (ii) that the PDT treatment with PS^{FAA} does not promote the production of immunosuppressives and pro-inflammatory cytokines (TGFβ, TNFα, IL-10) or decrease the secretion of immunoactivating ones (IL-2 and IFNγ). To summarize our results concerning the secretion of cytokines following PDT treatment, we can say that the PDT treatment with PS^{FAA} is able to modulate the inflammatory microenvironment of EOC by inhibiting the IL-6 secretion.

5. Conclusion

Until today, PDT showed some limits when applied at the clinical level due mainly to side effects linked to the lack of targeting of current PSs. Our work has shown that a PDT using a new PS coupled with a stable FAA hence ensuring FRα targeting overexpressed by OC cells, could be effective for OC treatment. Furthermore, this strategy using a PDT treatment with PS^{FAA}-PDT seems to induce a modulation of the inflammatory microenvironment by inhibiting the IL-6 cytokine secretion, which could limit the cancer progression, and thus avoiding relapses. An adjuvant treatment like PDT seems adequate in eliminating the microscopic intraperitoneal lesions and opening up new therapeutic perspectives in a cancer that is currently at a therapeutic stalemate. Finally, as peritoneum is also a common site of dissemination for other types of cancer overexpressing FRα (colorectal, gastric, esophageal, and hepatocellular cancers), and our new third-generation PS could be used to treat these malignancies.

Funding

This work was supported by two PhD grants funded by the French League Against Cancer for Léa Boidin, and the French Ministry of Higher Education, Research and Innovation for Morgane Moinard, and by one Post-PhD grant funded by the Regional Council of Lorraine and the University of Lorraine for Albert Moussaron.

CRediT authorship contribution statement

Léa Boidin: Writing – review & editing, Writing – original draft, Validation, Methodology, Investigation, Formal analysis, Conceptualization. **Morgane Moinard:** Writing – review & editing, Writing – original draft, Validation, Methodology, Investigation, Formal analysis, Conceptualization. **Albert Moussaron:** Writing – review & editing, Writing – original draft, Validation, Methodology, Investigation, Formal analysis, Conceptualization. **Margaux Merlier:** Investigation, Formal analysis. **Olivier Moralès:** Writing – review & editing, Writing – original draft, Validation, Methodology, Investigation, Formal analysis, Conceptualization. **Guillaume Paul Grolez:** Writing – review & editing, Writing – original draft, Validation, Methodology, Investigation, Formal analysis, Conceptualization. **Martha Baydoun:** Validation, Formal analysis, Conceptualization. **Amirah Mohd-Gazzali:** Writing – original draft, Supervision, Formal analysis. **Mohammad Hafizie Dianel Mohd Tazizi:** Writing – review & editing, Writing – original draft, Validation, Methodology, Investigation, Formal analysis, Conceptualization. **Hassan Hadi Abd Allah:** Validation, Investigation, Formal analysis. **Yohan Kerbage:** Supervision, Project administration, Conceptualization. **Philippe Arnoux:** Validation, Investigation, Formal analysis. **Samir Acherar:** Writing – review & editing, Writing – original draft, Validation, Supervision, Resources, Project administration, Conceptualization. **Céline Frochot:** Writing – review & editing, Writing – original draft, Visualization, Validation, Supervision, Resources, Project administration, Funding acquisition, Conceptualization. **Nadira Delhem:** Writing – review & editing, Writing – original draft, Visualization, Validation, Supervision, Resources, Project administration, Funding acquisition, Conceptualization.

Data availability

No data was used for the research described in the article.

Acknowledgments

We thank Dr. Xavier Thuru Head of the Integrative Chemistry-Biology Technical Facility, for the Microscale Thermophoresis experiments.

We thank the APPEL facility of LCPM, Université de Lorraine, for measurements, data processing and analysis, and providing of reports for publication: https://lcpm.univ-lorraine.fr/content/plateforme-appel-0

We acknowledge the SAMPL platform of LRGP for the photophysical studies.

Appendix A. Supplementary data

Supplementary data to this article can be found online at https://doi.org/10.1016/j.jconrel.2024.05.033.

References

[1] P. Gaona-Luviano, L.A. Medina-Gaona, K. Magaña-Pérez, Epidemiology of ovarian Cancer, Chin. Clin. Oncol. 9 (2020) 47, https://doi.org/10.21037/cco-20-34.
[2] S. Gupta, S. Nag, S. Aggarwal, A. Rauthan, N. Warrier, Maintenance therapy for recurrent epithelial ovarian Cancer: current therapies and future perspectives – a review, J. Ovarian Res. 12 (2019) 103, https://doi.org/10.1186/s13048-019-0579-0.
[3] B.M. Reid, J.B. Permuth, T.A. Sellers, Epidemiology of ovarian Cancer: a review, Cancer Biol. Med. 14 (2017) 9–32, https://doi.org/10.20892/j.issn.2095-3941.2016.0084.
[4] P. Giampaolino, V. Foreste, L. Della Corte, C. Di Filippo, G. Iorio, G. Bifulco, Role of biomarkers for early detection of ovarian Cancer recurrence, Gland Surg. 9 (2020) 1102–1111, https://doi.org/10.21037/gs-20-544.
[5] S. Kehoe, J. Hook, M. Nankivell, G.C. Jayson, H. Kitchener, T. Lopes, D. Luesley, T. Perren, S. Bannoo, M. Mascarenhas, et al., Primary chemotherapy versus primary surgery for newly diagnosed advanced ovarian Cancer (CHORUS): an open-label, randomised, controlled, Non-Inferiority Trial, Lancet 386 (2015) 249–257, https://doi.org/10.1016/S0140-6736(14)62223-6.

[6] K.C. Kurnit, G.F. Fleming, E. Lengyel, Updates and new options in advanced epithelial ovarian Cancer treatment, Obstet. Gynecol. 137 (2021) 108–121, https://doi.org/10.1097/AOG.0000000000004173.

[7] S. Pignata, C. Pisano, M. Di Napoli, S.C. Cecere, R. Tambaro, L. Attademo, Treatment of recurrent epithelial ovarian Cancer, Cancer 125 (Suppl. 24) (2019) 4609–4615, https://doi.org/10.1002/cncr.32500.

[8] H. Azaïs, A.-S. Vignion-Dewalle, M. Carrier, J. Augustin, E. Da Maïa, A. Penel, J. Belghiti, M. Nikpayam, C. Gonthier, L. Ziane, et al., Microscopic peritoneal residual disease after complete macroscopic Cytoreductive surgery for advanced high grade serous ovarian Cancer, J. Clin. Med. 10 (2020) E41, https://doi.org/10.3390/jcm10010041.

[9] A. Macciò, C. Madeddu, Inflammation and ovarian Cancer, Cytokine 58 (2012) 133–147, https://doi.org/10.1016/j.cyto.2012.01.015.

[10] A. Isobe, K. Sawada, Y. Kinose, C. Ohyagi-Hara, E. Nakatsuka, H. Makino, T. Ogura, T. Mizuno, N. Suzuki, E. Morii, et al., Interleukin 6 receptor is an independent prognostic factor and a potential therapeutic target of ovarian Cancer, PLoS One 10 (2015) e0118080, https://doi.org/10.1371/journal.pone.0118080.

[11] D. Lane, I. Matte, P. Garde-Granger, P. Bessette, A. Piché, Ascites IL-10 promotes ovarian Cancer cell migration, Cancer Microenviron. 11 (2018) 115–124, https://doi.org/10.1007/s12307-018-0215-3.

[12] A. Mustea, D. Könsgen, E.I. Braicu, C. Pirvulescu, P. Sun, D. Sofroni, W. Lichtenegger, J. Sehouli, Expression of IL-10 in patients with ovarian carcinoma, Anticancer Res. 26 (2006) 1715–1718.

[13] M. Plante, S.C. Rubin, G.Y. Wong, M.G. Federici, C.L. Finstad, G.A. Gastl, Interleukin-6 level in serum and ascites as a prognostic factor in patients with epithelial ovarian Cancer, Cancer 73 (1994) 1882–1888, https://doi.org/10.1002/1097-0142(19940401)73:7<1882::aid-cncr2820730718>3.0.co;2-r.

[14] M. Nowak, E. Glowacka, M. Szpakowski, K. Szyllo, A. Malinowski, A. Kulig, H. Tchorzewski, J. Wilczynski, Proinflammatory and immunosuppressive serum, ascites and cyst fluid cytokines in patients with early and advanced ovarian Cancer and benign ovarian tumors, Neuro Endocrinol. Lett. 31 (2010) 375–383.

[15] E.M. Dijkgraaf, M.J.P. Welters, J.W.R. Nortier, S.H. van der Burg, J.R. Kroep, Interleukin-6/Interleukin-6 receptor pathway as a new therapy target in epithelial ovarian Cancer, Curr. Pharm. Des. 18 (2012) 3816–3827, https://doi.org/10.2174/138161212802002797.

[16] J. Coward, H. Kulbe, P. Chakravarty, D. Leader, V. Vassileva, D.A. Leinster, R. Thompson, T. Schioppa, J. Nemeth, J. Vermeulen, et al., Interleukin-6 as a therapeutic target in human ovarian Cancer, Clin. Cancer Res. 17 (2011) 6083–6096, https://doi.org/10.1158/1078-0432.CCR-11-0945.

[17] R. Schneider, F. Schmitt, C. Frochot, Y. Fort, N. Lourette, F. Guillemin, J.-F. Müller, M. Barberi-Heyob, Design, synthesis, and biological evaluation of folic acid targeted Tetraphenylporphyrin as novel photosensitizers for selective photodynamic therapy, Bioorg. Med. Chem. 13 (2005) 2799–2808, https://doi.org/10.1016/j.bmc.2005.02.025.

[18] C. Donohoe, M.O. Senge, L.G. Arnaut, L.C. Gomes-da-Silva, Cell death in photodynamic therapy: from oxidative stress to anti-tumor immunity, Biochimica et Biophysica Acta (BBA) - reviews on Cancer 1872 (2019) 188308, https://doi.org/10.1016/j.bbcan.2019.07.003.

[19] R. Falk-Mahapatra, S.O. Gollnick, Photodynamic therapy and immunity: an update, Photochem. Photobiol. 96 (2020) 550–559, https://doi.org/10.1111/php.13253.

[20] G.M. van Dam, G. Themelis, L.M.A. Crane, N.J. Harlaar, R.G. Pleijhuis, W. Kelder, A. Sarantopoulos, J.S. de Jong, H.J.G. Arts, A.G.J. van der Zee, et al., Intraoperative tumor-specific fluorescence imaging in ovarian Cancer by folate receptor-? Targeting: first in-human results, Nat. Med. 17 (2011) 1315–1319, https://doi.org/10.1038/nm.2472.

[21] J.L. Tanyi, L.M. Randall, S.K. Chambers, K.A. Butler, I.S. Winer, C.L. Langstraat, E. S. Han, A.L. Vahrmeijer, H.S. Chon, M.A. Morgan, et al., A phase III study of Pafolacianine injection (OTL38) for intraoperative imaging of folate receptor-positive ovarian Cancer (study 006), J. Clin. Oncol. 41 (2023) 276–284, https://doi.org/10.1200/JCO.22.00291.

[22] M.R. Hamblin, Advances in Photodynamic Therapy: Basic, Translational, and Clinical, Artech House, 2008 (ISBN 978-1-59693-278-4.).

[23] W.F. Sindelar, T.F. DeLaney, Z. Tochner, G.F. Thomas, L.J. Dachoswki, P.D. Smith, W.S. Friauf, J.W. Cole, E. Glatstein, Technique of photodynamic therapy for disseminated intraperitoneal malignant neoplasms, Arch. Surg. 126 (1991) 318–324, https://doi.org/10.1001/archsurg.1991.01410270062011.

[24] T.F. Delaney, W.F. Sindelar, Z. Tochner, P.D. Smith, W.S. Friauf, G. Thomas, L. Dachowski, J.W. Cole, S.M. Steinberg, E. Glatstein, Phase I study of Debulking surgery and photodynamic therapy for disseminated intraperitoneal tumors, International J Radiation Oncology*Biology*Physics 25 (1993) 445–457, https://doi.org/10.1016/0360-3016(93)90066-5.

[25] S.M. Hahn, D.L. Fraker, R. Mick, J. Metz, T.M. Busch, D. Smith, T. Zhu, C. Rodriguez, A. Dimofte, F. Spitz, et al., A phase II trial of intraperitoneal photodynamic therapy for patients with peritoneal Carcinomatosis and Sarcomatosis, Clin. Cancer Res. 12 (2006) 2517–2525, https://doi.org/10.1158/1078-0432.CCR-05-1625.

[26] M. Moinard, J. Augustin, M. Carrier, E. Da Maïa, A. Penel, J. Belghiti, M. Nikpayam, C. Gonthier, G. Canlorbe, S. Acherar, et al., Residual microscopic peritoneal metastases after macroscopic complete Cytoreductive surgery for advanced high-grade serous ovarian carcinoma: a target for folate receptor targeted photodynamic therapy? Pharmaceuticals (Basel) 15 (2022) 1034, https://doi.org/10.3390/ph15081034.

[27] A. Stallivieri, L. Colombeau, G. Jetpisbayeva, A. Moussaron, B. Myrzakhmetov, P. Arnoux, S. Acherar, R. Vanderesse, C. Frochot, Folic acid conjugates with photosensitizers for Cancer targeting in photodynamic therapy: synthesis and Photophysical properties, Bioorg. Med. Chem. 25 (2017) 1–10, https://doi.org/10.1016/j.bmc.2016.10.004.

[28] M. Baydoun, O. Moralès, C. Frochot, C. Ludovic, B. Leroux, E. Thecua, L. Ziane, A. Grabarz, A. Kumar, C. de Schutter, et al., Photodynamic therapy using a new folate receptor-targeted photosensitizer on peritoneal ovarian Cancer cells induces the release of extracellular vesicles with Immunoactivating properties, J. Clin. Med. 9 (2020), https://doi.org/10.3390/jcm9041185.

[29] M. Baydoun, L. Boidin, B. Leroux, A.-S. Vignion-Dewalle, A. Quilbe, G.P. Grolez, H. Azaïs, C. Frochot, O. Moralès, N. Delhem, Folate receptor targeted photodynamic therapy: a novel way to stimulate anti-tumor immune response in intraperitoneal ovarian Cancer, Int. J. Mol. Sci. 24 (2023) 11288, https://doi.org/10.3390/ijms241411288.

[30] A.M. Gazzali, M. Lobry, L. Colombeau, S. Acherar, H. Azaïs, S. Mordon, P. Arnoux, F. Baros, R. Vanderesse, C. Frochot, Stability of folic acid under several parameters, Eur. J. Pharm. Sci. 93 (2016) 419–430, https://doi.org/10.1016/j.ejps.2016.08.045.

[31] B. Myrzakhmetov, P. Arnoux, S. Mordon, S. Acherar, I. Tsoy, C. Frochot, Photophysical properties of Protoporphyrin IX, Pyropheophorbide-a and Photofrin® in different conditions, Pharmaceuticals (Basel) 14 (2021) 138, https://doi.org/10.3390/ph14020138.

[32] E. Thécua, L. Ziane, G.P. Grolez, A. Fagart, A. Kumar, B. Leroux, G. Baert, P. Deleporte, M. Vermandel, A.-S. Vignion-Dewalle, et al., A warp-knitted light-emitting fabric-based device for in vitro photodynamic therapy: description, characterization, and application on human Cancer cell lines, Cancers (Basel) 13 (2021) 4109, https://doi.org/10.3390/cancers13164109.

[33] M.G. Al-Thiabat, A.M. Gazzali, N. Mohtar, V. Murugaiyah, E.E. Kamarulzaman, B. K. Yap, N.A. Rahman, R. Othman, H.A. Wahab, Conjugated β-Cyclodextrin enhances the affinity of folic acid towards FRα: molecular dynamics study, Molecules 26 (2021) 5304, https://doi.org/10.3390/molecules26175304.

[34] L. Larue, T. Moussounda Moussounda Koumba, N. Le Breton, B. Vileno, P. Arnoux, V. Jouan-Hureaux, C. Boura, G. Audran, R. Bikanga, S.R.A. Marque, et al., Design of a Targeting and Oxygen-Independent Platform to improve photodynamic therapy: a proof of concept, ACS Appl. Bio Mater. 4 (2021) 1330–1339, https://doi.org/10.1021/acsabm.0c01227.

[35] A. Stallivieri, F. Baros, G. Jetpisbayeva, B. Myrzakhmetov, C. Frochot, The interest of folic acid in targeted photodynamic therapy, Curr. Med. Chem. 22 (2015) 3185–3207, https://doi.org/10.2174/0929867322666150729113912.

[36] J.M. Medina-Castro, A. Ruiz-DeLeón, Role of Hyperthermic intraperitoneal chemotherapy in ovarian Cancer, Chin. Clin. Oncol. 9 (2020) 44, https://doi.org/10.21037/cco-20-49.

[37] P. Amate, C. Huchon, A.L. Dessapt, C. Bensaid, J. Medioni, M.-A. Le Frère Belda, A.-S. Bats, F.R. Lécuru, Ovarian Cancer: sites of recurrence, Int. J. Gynecol. Cancer 23 (2013) 1590–1596, https://doi.org/10.1097/IGC.0000000000000007.

[38] B. Huang, X. Lang, X. Li, The role of IL-6/JAK2/STAT3 signaling pathway in cancers, Front. Oncol. 12 (2022) 1023177, https://doi.org/10.3389/fonc.2022.1023177.

[39] L. Browning, M.R. Patel, E.B. Horvath, K. Tawara, C.L. Jorcyk, IL-6 and ovarian Cancer: inflammatory cytokines in promotion of metastasis, Cancer Manag. Res. 10 (2018) 6685–6693, https://doi.org/10.2147/CMAR.S179189.

[40] N.E. Martin, S.M. Hahn, Interstitial photodynamic therapy for prostate Cancer: a developing modality, Photodiagn. Photodyn. Ther. 1 (2004) 123–136, https://doi.org/10.1016/S1572-1000(04)00037-7.

[41] Ogawa, K.; Kobuke, Y. Recent Advances in Two-Photon Photodynamic Therapy. Anti Cancer Agents Med. Chem. 8, 269–279.

[42] J.S. Souris, L. Leoni, H.J. Zhang, A. Pan, E. Tanios, H.-M. Tsai, I.V. Balyasnikova, M. Bissonnette, C.-T. Chen, X-ray activated Nanoplatforms for deep tissue photodynamic therapy, Nanomaterials 13 (2023) 673, https://doi.org/10.3390/nano13040673.

[43] H. Abrahamse, M.R. Hamblin, New photosensitizers for photodynamic therapy, Biochem. J. 473 (2016) 347–364, https://doi.org/10.1042/BJ20150942.

[44] F. Moret, E. Reddi, Strategies for optimizing the delivery to tumors of macrocyclic photosensitizers used in photodynamic therapy (PDT), J. Porphyrins Phthalocyanines 21 (2017) 239–256, https://doi.org/10.1142/S1088424617300014.

[45] A, A.; Ghosh, M, Recent Developments of Porphyrin Photosensitizers in Photodynamic Therapy, 2023.

[46] C.-C. Albu, M.-A. Bencze, A.-O. Dragomirescu, I. Suciu, M. Tănase, Ş.-D. Albu, E.-A. Russu, E. Ionescu, Folic acid and its role in Oral health: a narrative review, Processes 2023 (1994) 11, https://doi.org/10.3390/pr11071994.

[47] A. Narmani, M. Rezvani, B. Farhood, P. Darkhor, J. Mohammadnejad, B. Amini, S. Refahi, N. Abdi Goushbolagh, Folic acid functionalized nanoparticles as pharmaceutical carriers in drug delivery systems, Drug Dev. Res. 80 (2019) 404–424, https://doi.org/10.1002/ddr.21545.

[48] E.I. Sega, P.S. Low, Tumor detection using folate receptor-targeted imaging agents, Cancer Metastasis Rev. 27 (2008) 655–664, https://doi.org/10.1007/s10555-008-9155-6.

[49] L. Wagner, B. Kenzhebayeva, B. Dhaini, S. Boukhlef, A. Moussaron, S. Mordon, C. Frochot, C. Collet, S. Acherar, Folate-based radiotracers for nuclear imaging and radionuclide therapy, Coord. Chem. Rev. 470 (2022) 214702, https://doi.org/10.1016/j.ccr.2022.214702.

[50] J.A. Ledermann, S. Canevari, T. Thigpen, Targeting the folate receptor: diagnostic and therapeutic approaches to personalize Cancer treatments, Ann. Oncol. 26 (2015) 2034–2043, https://doi.org/10.1093/annonc/mdv250.

[51] A. Cheung, H.J. Bax, D.H. Josephs, K.M. Ilieva, G. Pellizzari, J. Opzoomer, J. Bloomfield, M. Fittall, A. Grigoriadis, M. Figini, et al., Targeting folate receptor

alpha for Cancer treatment, Oncotarget 7 (2016) 52553–52574, https://doi.org/10.18632/oncotarget.9651.
[52] W. Xia, P.S. Low, Folate-targeted therapies for Cancer, J. Med. Chem. 53 (2010) 6811–6824, https://doi.org/10.1021/jm100509v.
[53] Y. Wu, F. Li, X. Zhang, Z. Li, Q. Zhang, W. Wang, D. Pan, X. Zheng, Z. Gu, H. Zhang, et al., Tumor microenvironment-responsive PEGylated heparin-Pyropheophorbide-a Nanoconjugates for photodynamic therapy, Carbohydr. Polym. 255 (2021) 117490, https://doi.org/10.1016/j.carbpol.2020.117490.
[54] X. Li, S. Kolemen, J. Yoon, E.U. Akkaya, Activatable photosensitizers: agents for selective photodynamic therapy, Adv. Funct. Mater. 27 (2017) 1604053, https://doi.org/10.1002/adfm.201604053.
[55] W. Li, S. Tan, Y. Xing, Q. Liu, S. Li, Q. Chen, M. Yu, F. Wang, Z. Hong, cRGD peptide-conjugated Pyropheophorbide-a photosensitizers for tumor targeting in photodynamic therapy, Mol. Pharm. 15 (2018) 1505–1514, https://doi.org/10.1021/acs.molpharmaceut.7b01064.
[56] F. Rancan, M. Helmreich, A. Mölich, E.A. Ermilov, N. Jux, B. Röder, A. Hirsch, F. Böhm, Synthesis and in vitro testing of a Pyropheophorbide-a-fullerene Hexakis adduct Immunoconjugate for photodynamic therapy, Bioconjug. Chem. 18 (2007) 1078–1086, https://doi.org/10.1021/bc0603337.
[57] E.A. Ermilov, S. Tannert, T. Werncke, M.T.M. Choi, D.K.P. Ng, B. Röder, Photoinduced Electron and Energy Transfer in a New Porphyrin–Phthalocyanine Triad, Chem. Phys. 328 (2006) 428–437, https://doi.org/10.1016/j.chemphys.2006.07.040.
[58] B. Röder, M. Büchner, I. Rückmann, M.O. Senge, Correlation of Photophysical parameters with macrocycle distortion in porphyrins with graded degree of saddle distortion, Photochem. Photobiol. Sci. 9 (2010) 1152–1158, https://doi.org/10.1039/C0PP00107D.
[59] M. Bagnoli, A. Tomassetti, M. Figini, S. Flati, V. Dolo, S. Canevari, S. Miotti, Downmodulation of Caveolin-1 expression in human ovarian carcinoma is directly related to α-folate receptor overexpression, Oncogene 19 (2000) 4754, https://doi.org/10.1038/sj.onc.1203839.
[60] M.K.Y. Siu, D.S.H. Kong, H.Y. Chan, E.S.Y. Wong, P.P.C. Ip, L. Jiang, H.Y.S. Ngan, X.-F. Le, A.N.Y. Cheung, Paradoxical impact of two folate receptors, FRα and RFC, in ovarian Cancer: effect on cell proliferation, Invasion and Clinical Outcome, PLoS One 7 (2012) e47201, https://doi.org/10.1371/journal.pone.0047201.
[61] A.S. Wibowo, M. Singh, K.M. Reeder, J.J. Carter, A.R. Kovach, W. Meng, M. Ratnam, F. Zhang, C.E. Dann, Structures of human folate receptors reveal biological trafficking states and diversity in folate and Antifolate recognition, Proc. Natl. Acad. Sci. USA 110 (2013) 15180–15188, https://doi.org/10.1073/pnas.1308827110.
[62] C. Chen, J. Ke, X.E. Zhou, W. Yi, J.S. Brunzelle, J. Li, E.-L. Yong, H.E. Xu, K. Melcher, Structural basis for molecular recognition of folic acid by folate receptors, Nature 500 (2013) 486–489, https://doi.org/10.1038/nature12327.
[63] E. Nogueira, M.P. Sárria, N.G. Azoia, E. Antunes, A. Loureiro, D. Guimarães, J. Noro, A. Rollett, G. Guebitz, A. Cavaco-Paulo, Internalization of methotrexate conjugates by folate receptor-α, Biochemistry 57 (2018) 6780–6786, https://doi.org/10.1021/acs.biochem.8b00607.
[64] M. Kobayashi, C. Salomon, J. Tapia, S.E. Illanes, M.D. Mitchell, G.E. Rice, Ovarian Cancer cell invasiveness is associated with discordant Exosomal sequestration of Let-7 miRNA and miR-200, J. Transl. Med. 12 (2014) 4, https://doi.org/10.1186/1479-5876-12-4.
[65] P. Mroz, M.R. Hamblin, The immunosuppressive side of PDT, Photochem. Photobiol. Sci. 10 (2011) 751–758, https://doi.org/10.1039/c0pp00345j.
[66] P. Mroz, J.T. Hashmi, Y.-Y. Huang, N. Lange, M.R. Hamblin, Stimulation of anti-tumor immunity by photodynamic therapy, Expert Rev. Clin. Immunol. 7 (2011) 75–91, https://doi.org/10.1586/eci.10.81.
[67] J.A.V. Morais, L.R. Almeida, M.C. Rodrigues, R.B. Azevedo, L.A. Muehlmann, The induction of immunogenic cell death by photodynamic therapy in B16F10 cells in vitro is effected by the concentration of the photosensitizer, Photodiagn. Photodyn. Ther. 35 (2021) 102392, https://doi.org/10.1016/j.pdpdt.2021.102392.
[68] M.R. Hamblin, H. Abrahamse, Factors affecting photodynamic therapy and anti-tumor immune response, Anti Cancer Agents Med. Chem. 21 (2021) 123–136, https://doi.org/10.2174/1871520620666200318101037.
[69] R. Zhang, D.M. Roque, J. Reader, J. Lin, Combined inhibition of IL-6 and IL-8 pathways suppresses ovarian Cancer cell viability and migration and tumor growth, Int. J. Oncol. 60 (2022) 50, https://doi.org/10.3892/ijo.2022.5340.
[70] N. Kolomeyevskaya, K.H. Eng, A.N.H. Khan, K.S. Grzankowski, K.L. Singel, K. Moysich, B.H. Segal, Cytokine profiling of ascites at primary surgery identifies an interaction of tumor necrosis factor-α and Interleukin-6 in predicting reduced progression-free survival in epithelial ovarian Cancer, Gynecol. Oncol. 138 (2015) 352–357, https://doi.org/10.1016/j.ygyno.2015.05.009.
[71] D.R. Minor, S.P. Moores, J.K. Chan, Prolonged survival after intraperitoneal Interleukin-2 immunotherapy for recurrent ovarian Cancer, Gynecol Oncol Rep 22 (2017) 43–44, https://doi.org/10.1016/j.gore.2017.09.009.
[72] A.H. Gao, Y.R. Hu, W.P. Zhu, IFN-γ inhibits ovarian Cancer progression via SOCS1/JAK/STAT signaling pathway, Clin. Transl. Oncol. 24 (2022) 57–65, https://doi.org/10.1007/s12094-021-02668-9.
[73] J. Coward, H. Kulbe, P. Chakravarty, D. Leader, V. Vassileva, D.A. Leinster, R. Thompson, T. Schioppa, J. Nemeth, J. Vermeulen, N. Singh, N. Avril, J. Cummings, E. Rexhepaj, K. Jirström, W.M. Gallagher, D.J. Brennan, I. A. McNeish, F.R. Balkwill, Interleukin-6 as a therapeutic target in human ovarian cancer, Clin Cancer Res 17 (18) (2011) 6083–6096, https://doi.org/10.1158/1078-0432.CCR-11-0945. Epub 2011 Jul 27. PMID: 21795409; PMCID: PMC3182554.